

**VIIRS Leaf Area Index (LAI) and Fraction of Photosynthetically Active
Radiation Absorbed by Vegetation (FPAR) Product Algorithm Theoretical
Basis Document (ATBD)**

Principal Investigator: Ranga B. Myneni
Correspondence e-mail address: rmyneni@bu.edu

Version 1.1
April 2018

This document was developed by Taejin Park, Kai Yan, Chi Chen, Baodong Xu,
Yuri Knyazikhin and Ranga Myneni

Department of Earth and Environment
Boston University

Change History Log

<i>Revision</i>	<i>Effective Date</i>	<i>Description of Changes</i>
V1.0	06/20/2017	First Draft based on MODIS ATBD and VIIRS Algorithm Deployment
V1.1	04/17/2018	Ancillary information in the product has been updated

Table of Content

1. Introduction	6
1.1. Science/Applications Rationale for the Product.....	6
1.2. Intended User Community.....	9
2. Algorithm	10
2.1. Technical Background and Heritage.....	10
2.2. Overview of the Algorithm.....	11
2.3. Radiation Transport in a Canopy.....	14
2.4. Theory of spectral invariants	17
2.5. Inverse problem and stabilized precision (Observation and model).....	18
2.6. Characteristics of Land Surface BRFs.....	22
<i>2.6.1. Spectral Characteristic</i>	<i>22</i>
<i>2.6.2. Comparability of BRFs</i>	<i>23</i>
2.7. Solving the optimization problem.....	26
2.8. Backup Algorithm.....	33
3. Product	37
3.1. Product Description	37
3.2. Product Input	40
<i>3.2.1 Spectral Bands</i>	<i>40</i>
<i>3.2.2 Masks, Thresholds and Ancillary Data</i>	<i>40</i>
3.3. Production Logic and Data Flow	42
3.3.1. LAI & FPAR Algorithm - Daily Logic (PGE-533)	42
3.3.2. LAI & FPAR Algorithm - 8-day Compositing Logic (PGE-534)	43
4. Product Accuracy/Uncertainty.....	45
4.1. Validation Approach.....	45
<i>4.1.1. Direct Validation.....</i>	<i>46</i>
<i>4.1.3. Indirect Validation</i>	<i>48</i>
4.2. Preliminary Assessment	49
<i>4.2.1. Direct Validation.....</i>	<i>49</i>
4.2.2. Indirect Validation (Consistency Evaluation).....	49
5. Data Formats.....	57
5.1. Formats	57
5.2. QC Metadata	57
5.3. Spatial Projection	59
6. Product Publications	60
7. References.....	61

Abbreviation

AMI	Algorithm Match Index
APU	Accuracy, Precision and Uncertainty
ATBD	Algorithm Theoretical Basis Documents
AVHRR	Advanced Very-high Resolution Radiometer
BELMANIP	BEenchmark Land Multisite ANalysis and Intercomparison of Products
BRDF	Bidirectional Reflectance Distribution Function
BRF	Bidirectional Reflectance Factor
BS	Black Soil
C6	Collection 6
CEOS	Committee on Earth Observation Satellites
CV	Coefficient of Variation
DHR	Directional Hemispherical Reflectance
DLAI	Dispersion of Leaf Area Index
DNB	Day Night Band
DOY	Day of Year
ECS	EOSDIS Core System
ECV	Essential Climate Variable
EDR	Environmental Data Record
EOS	Earth Observing System
EOSDIS	Earth Observing System Data and Information System
ESDR	Earth Science Data Record
ESDT	Earth Science Data Type
ESU	Elementary Sampling Unit
EVI	Enhanced Vegetation Index
FPAR	Fraction of Photosynthetically Active Radiation
FWHM	Full Width at Half Maximum
GCOS	Global Climate Observing System
HDF	Hierarchical Data Format
IRAD	Internal Research and Development
JPSS	Joint Polar Satellite System
L2G	Level 2 Gridded
LAD	Leaf Area Density
LAI	Leaf Area Index
LC	Land Cover
LP DAAC	Land Process Distributed Active Archive Center
LPV	Land Product Validation
LUT	Look Up Table
MALIBU	Multi AngLe Imaging Bidirectional Reflectance Distribution Function sUAS
MODIS	Moderate Resolution Imaging Spectroradiometer

NASA	National Aeronautics and Space Administration
NDVI	Normalized Difference Vegetation Index
NGO	Non Government Organization
NIR	Near Infra-Red
NOAA	National Oceanic and Atmospheric Administration
NPOESS	National Polar-orbiting Operational Environmental Satellite System
PGE	Product Generation Executable
QA	Quality Assurance
QC	Quality Control
RI	Retrieval Index
RMSE	Root Mean Squared Error
RSP	Relative Stabilized Precision
RSR	Relative Spectral Response
RT (RTM)	Radiative Transfer (Radiative Transfer Model)
S	Soil
SCF	Science Computing Facilities
SDR	Sensor Data Record
SIPS	Science Investigator Processing System
SNPP	Suomi National Polar-orbiting Partnership
SPOT	Satellite Pour l'Observation de la Terre Vegetation
SR	Surface Reflectance
SSA	Single Scattering Albedo
UAS	Unmanned Aircraft System
VIIRS	Visible/Infrared Imager Radiometer Suite
WGCV	Working Group on Calibration & Validation

1. Introduction

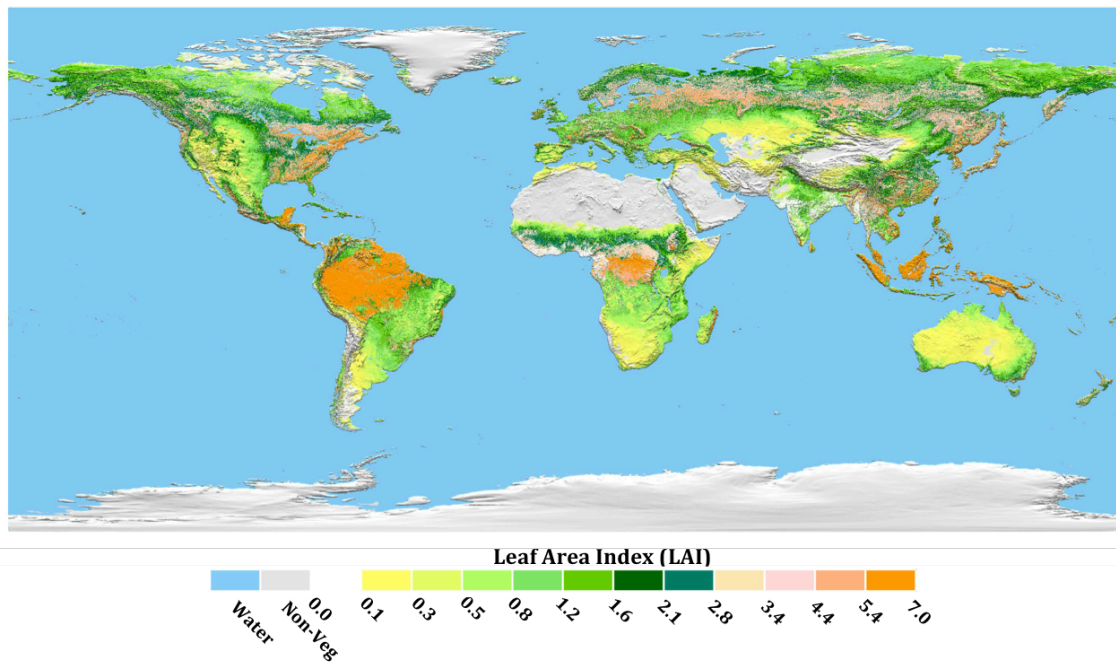
1.1. Science/Applications Rationale for the Product

Investigating a range of ecological responses to changes in climate, chemical composition of the atmosphere and terrestrial plant communities across the globe is crucial to understanding the current state of the Earth's systems and to diagnosing the magnitude and direction of their changes. Large-scale modeling has drawn the attention of a broad range of scientific communities as it can provide an effective means to simulating the interactions between the biosphere, atmosphere, hydrosphere etc. and the causal relations for observed phenomena (Taylor et al., 2012). Green leaves are the primary interface for the exchange of fluxes of energy, mass (e.g., water, nutrient and CO₂) and momentum between the terrestrial surface and the planetary boundary layer (Richardson et al., 2012). Thus most ecosystem and climate models introduce the area of leaves as a key state parameter describing the interactions between the biosphere and atmosphere. The most common measure of the area of leaves is the leaf area index (LAI), which is generally defined as one half of the total leaf surface area divided by the ground area (Chen and Black, 1992).

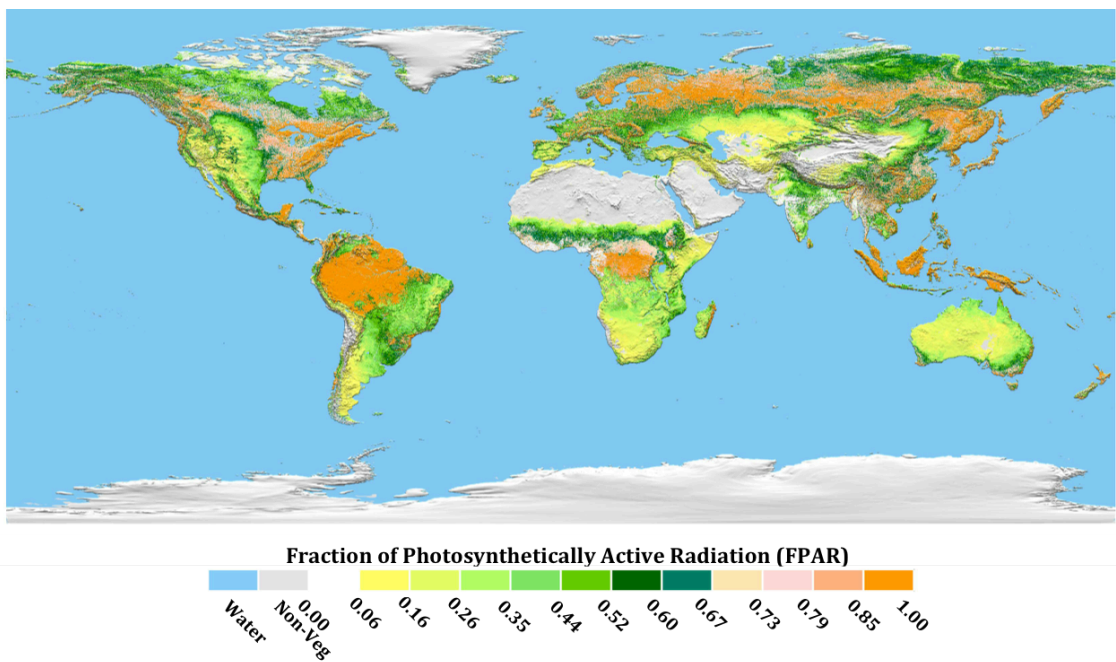
Another key parameter that characterizes the energy absorption capacity of vegetation is the fraction of photosynthetically active radiation (0.4–0.7 μm , FPAR) absorbed by the vegetation canopy. FPAR depends on the incident radiation field, architecture and absorption, reflectance and transmission spectra of the canopy as well as the reflectance of the soil and/or understory background. It is one of the fundamental parameters used to estimate net primary production and for modeling of terrestrial carbon processes (Sellers et al., 1986; Knorr and Kattge, 2005). Similar to LAI, FPAR has also been identified as one of the fundamental terrestrial state variables in global models of climate, hydrology, biogeochemistry and ecology (Sellers et al., 1997). Therefore these variables that describe vegetation canopy structure and its energy absorption capacity are required by many of the Earth Observing System (EOS) Interdisciplinary Projects (Myneni et al., 1997). Indeed, LAI/FPAR data has been acknowledged as a key Earth Science Data Record (ESDR) by the NASA Earth Science Division (Bontempi, 2015), and an Essential Climate Variable (ECV) by the Global Climate Observing System (GCOS) (GCOS, 2006).

The problem of accurately evaluating the exchange of carbon between the atmosphere and the terrestrial vegetation requires special attention. In order to quantitatively and accurately model global dynamics of these processes, differentiate short-term from long-term trends, as well as to distinguish regional from global phenomena, these two parameters, LAI and FPAR, must be collected often for a long period of time and should represent every region of the Earth's lands. Satellite remote sensing can serve as the most effective means for collecting global data on a regularly basis. Thus, efforts from the scientific community on developing global LAI/FPAR data using satellite observation have been made in last few decades (Knyazikhin et al., 1998a; Myneni et al., 2002; Zhu et al., 2013; Baret et al., 2013).

In particular, the ground-breaking Earth Observing System (EOS) Moderate Resolution Imaging Spectroradiometer (MODIS) sensor onboard Terra and Aqua satellites provided an opportunity for opening a new horizon of global LAI/FPAR products (Figure 1-1) (Myneni et al., 2002). A well-matured latest version (Collection 6) of global LAI/FPAR data set (since February 2000) from this sensor is freely available and much in use by the wide scientific, public and private user communities (Yan et al., 2016a; Yan et al., 2016b). As Terra and Aqua MODIS sensors will likely be terminated (Terra and Aqua MODIS have far exceeded their design life, 6 years, and have a strong chance of operating successfully into the early 2020s.), the Visible/Infrared Imager Radiometer Suite (VIIRS) instrument onboard the Suomi National Polar-orbiting Partnership (SNPP) and Joint Polar Satellite System (JPSS) has inherited the scientific roles of MODIS (Justice et al., 2013). The first VIIRS sensor onboard the SNPP platform was successfully launched in October 2011. Therefore, developing consistent LAI/FPAR data sets from these new sensors to continue the MODIS record is a high priority. This document primarily aims to describe the theoretical basis of proposed and developed global VIIRS LAI/FPAR product algorithm. Furthermore, as the ultimate goal lies in continuing global LAI/FPAR ESDR production as a successor to EOS MODIS, explicit consistency evaluation between VIIRS and MODIS is documented herein.



(A)



(B)

Figure 1-1. Global color-coded maps of Terra MODIS Collection 6 LAI (upper panel, A) and FPAR (lower panel, B). These maps were generated from nearly 16 years of Terra MODIS data (Only August datasets were used to calculate long-term climatology). Leaf area index (LAI) is defined as the one-sided green leaf area per unit ground area in broadleaf canopies and as one-half the total needle surface area per unit ground area in coniferous canopies. FPAR is defined as the fraction of incident photosynthetically active radiation (400–700 nm) absorbed by the green elements of a vegetation canopy. Both quantities are dimensionless.

1.2. Intended User Community

Remotely sensed global vegetation canopy LAI/FPAR products have been widely used by following user communities - (a) Scientific: modelers of climate, biogeochemistry, ecology, hydrology, crop production, etc.; (b) Public: meteorological organizations, deforestation, drought and desertification monitoring organizations, rapid response systems, pest risk evaluation companies, NGOs (Non-Governmental Organization) and governments (for the implementation and potential verification of compliance of international treaties); and (c) Private: international agriculture, forestry & insurance companies, traders, etc.

2. Algorithm

2.1. Technical Background and Heritage

Several different algorithmic approaches for estimating LAI/FPAR using remotely sensed surface reflectance measurements have been developed and widely used. The approaches can be conceptually categorized as: (a) Empirical approaches that are based on relationships between vegetation indices and (b) Physical approaches that are based on the physics of radiation interaction with elements of a canopy and transport within the vegetative medium.

For the empirical approaches, the Normalized Difference Vegetation Index (NDVI) is one of the most widely used vegetation index to infer LAI or FPAR (e.g., [Asrar et al., 1984](#)). These relationships are generally sensitive to soil background, leaf optical properties, the orientation and spatial distribution of leaves in a canopy and the general architecture of vegetation stands within the spatial scale of measurements ([Myneni et al., 1997](#)). However, the empirical approaches tend to be site-, time-, and species-specific, and are therefore not well suited for large-scale operational use ([Houborg et al., 2007](#)).

Physical model based approaches provide a linkage between biophysical variables and vegetation canopy reflectances at different wavelengths ([Knyazikhin et al., 1998a](#)). These methods can be categorized into four broad groups: (1) radiative transfer models ([Knyazikhin et al., 1998a](#)), (2) geometric-optical models (Li and Strahler, 1992), (3) hybrid models that incorporate both radiative transfer as well as geometric-optics ([Li et al., 1995](#)), and (4) computer simulation models (e.g., Monte-Carlo simulation) ([Ross and Marshak, 1988](#)). The methods involve iterative techniques and are thus computationally intensive for operational use. But, methods to alleviate this have also been developed, e.g., use of Look Up Tables (LUT) ([Knyazikhin et al., 1999](#)).

The VIIRS LAI/FPAR algorithm is based on a long heritage of legacy operational algorithms and theoretical research foundation. Two key heritages are (a) a well-matured 17-year long MODIS LAI/FPAR operational algorithm which is based on 3D-radiative transfer model and LUT, and (b) a physically proven algorithm for achieving inter-sensor consistency. Details can be found in the rest of [Section 2](#).

2.2. Overview of the Algorithm

The VIIRS LAI/FPAR algorithm has benefitted from the heritage of the MODIS operational algorithm. The algorithm retrieves LAI and FPAR values given sun and view directions, Bidirectional Reflectance Factor (BRF) for each spectral band, uncertainties (i.e., relative stabilized precision, Wang et al., 2001) in input BRFs, and land cover classes based on a 8-biome classification map (Myneni et al., 2002; Yang et al., 2006). The operational VIIRS LAI/FPAR algorithm consists of a main algorithm that is based on 3D RT equation. By describing the photon transfer process, this algorithm links surface spectral BRFs to both structural and spectral parameters of the vegetation canopy and soil (Myneni and Ross, 1991; Ross, 2012). Given atmosphere-corrected BRFs and their uncertainties, the algorithm finds candidates of LAI and FPAR by comparing observed and modeled BRFs that are stored in biome type specific LUTs. All canopy/soil patterns for which observed and modeled BRFs differ within biome-specified thresholds of uncertainties (e.g., 30% and 15% for red and near-infrared bands, respectively, for forest biomes) are considered candidate solutions and the mean values of LAI and FPAR from these solutions are reported as outputs (Figure 2-1). The mean and dispersion of LAI/FPAR candidates are reported as retrieval and its reliability, respectively. The law of energy conservation and the theory of spectral invariance are two important features of this main algorithm (Knyazikhin et al., 1999).

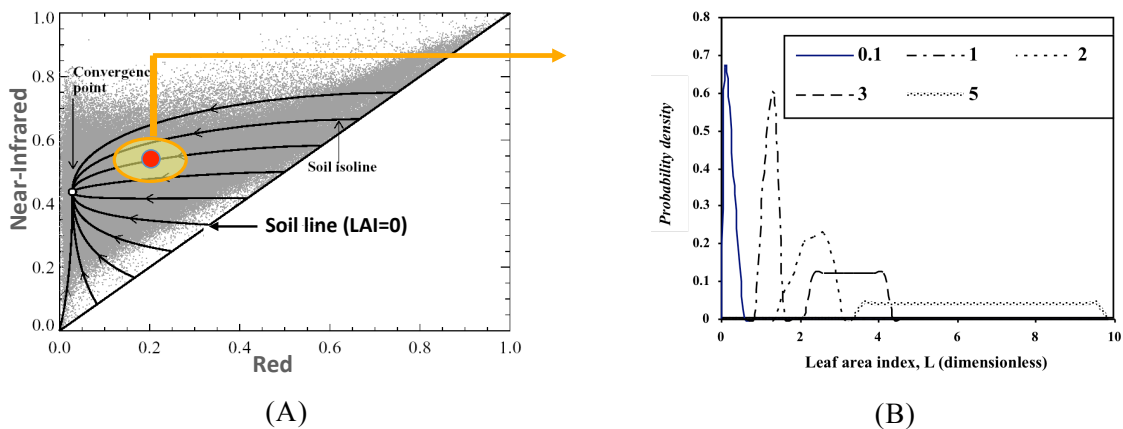


Figure 2-1. Schematic illustration of the main algorithm. (A) Distribution of vegetated pixels with respect to their reflectances at red and near-infrared (NIR) spectral bands. A point on the red-NIR plane and an area about it (yellow ellipse defined by a χ^2 distribution) are treated as the measured BRF at a given sun-sensor geometry and its uncertainty. Each combination of canopy/soil parameters and corresponding FPAR values for which modeled reflectances belong to the ellipse is an acceptable solution. (B) Density distribution function of acceptable solutions. Shown is solution density distribution function of LAI for five different pixels. The mean LAI and its dispersion (STD LAI) are taken as the LAI retrieval and its uncertainty. The figures are quoted from Knyazikhin et al. (1999).

The main algorithm may fail to localize a solution if uncertainties of input BRFs are larger than threshold values or due to deficiencies of the RT model that result in incorrect simulated BRFs. In such cases, a backup empirical method based on relations between NDVI and LAI/FPAR (Myneni et al., 1994; Knyazikhin et al., 1998a) is utilized to output LAI/FPAR with relatively poor quality—this is called the backup algorithm. Figure 2-2 demonstrates the distributions of the retrieved LAI and FPAR values with respect to the NDVI in the case of savanna biome showing the foundation of the backup algorithm using the latest version of VIIRS surface reflectance and LAI/FPAR algorithm. Panel C in Figure 2-2 show scatter plots of input reflectance data from successful and unsuccessful retrievals in the red and near-infrared space. This distribution provides insight on where and why the algorithm failed.

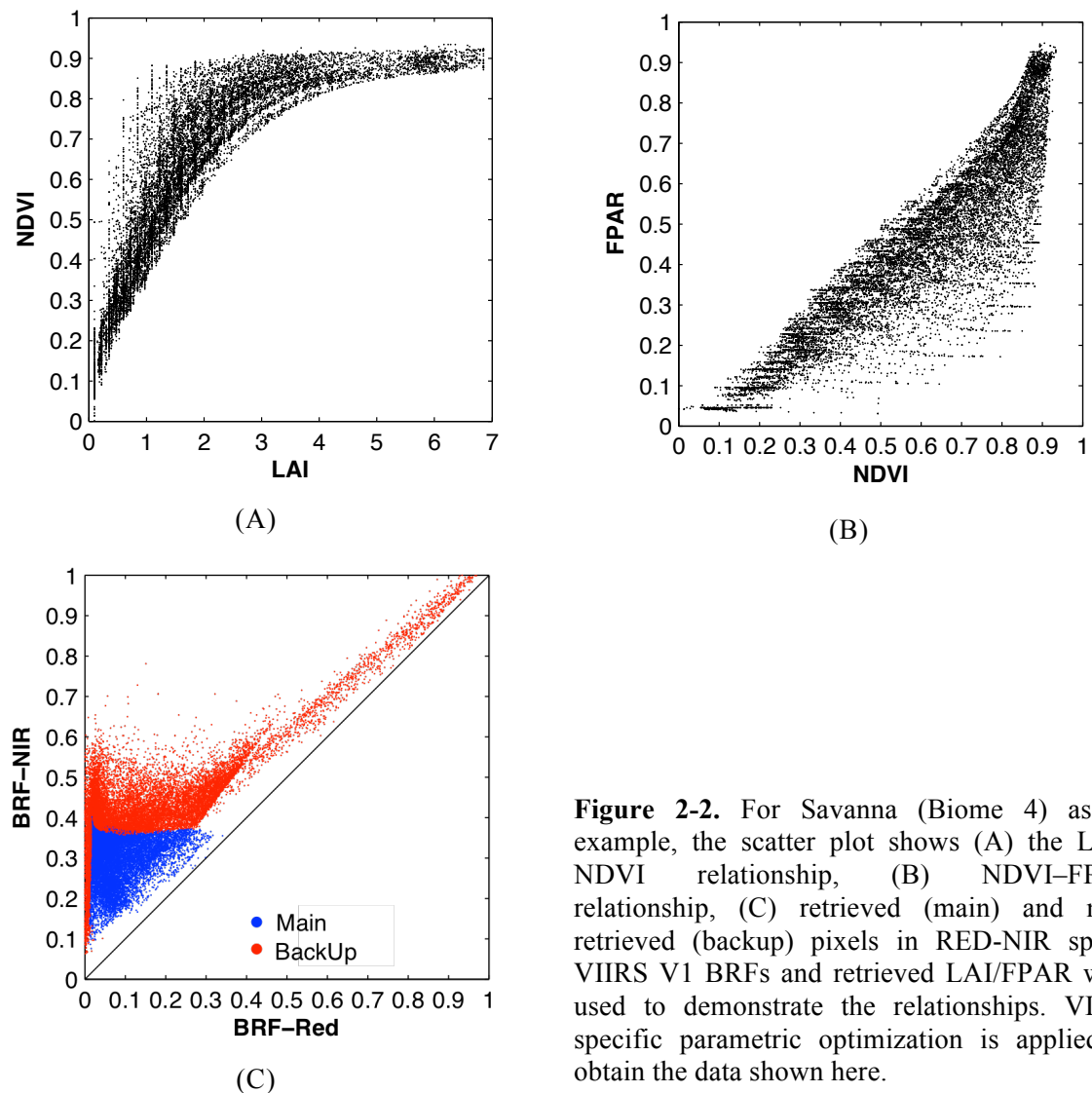


Figure 2-2. For Savanna (Biome 4) as an example, the scatter plot shows (A) the LAI–NDVI relationship, (B) NDVI–FPAR relationship, (C) retrieved (main) and non-retrieved (backup) pixels in RED-NIR space. VIIRS V1 BRFs and retrieved LAI/FPAR were used to demonstrate the relationships. VIIRS specific parametric optimization is applied to obtain the data shown here.

The algorithm currently requires: (a) atmospherically corrected surface reflectances at Red and NIR bands, and (b) an 8-biome Land Cover (LC) classification map distinguishing the following biomes types: (1) grasses and cereal crops, (2) shrubs, (3) broadleaf crops, (4) savannas, (5) evergreen broadleaf forests, (6) deciduous broadleaf forests, (7) evergreen needle leaf forests, (8) deciduous needle leaf forests (Figure 2-3). These biomes span structural variations along the horizontal and vertical dimensions, canopy height, leaf type, soil brightness and climate space of herbaceous and woody vegetation globally (Table 2-1). The biome map reduces the number of unknowns of the inverse problem through the use of simplifying assumptions (e.g., biome specific models of leaf orientation distributions; [Knyazikhin et al., 1998a](#)) and standard constants (e.g., biome-specific leaf and soil optical properties at given wavelengths).

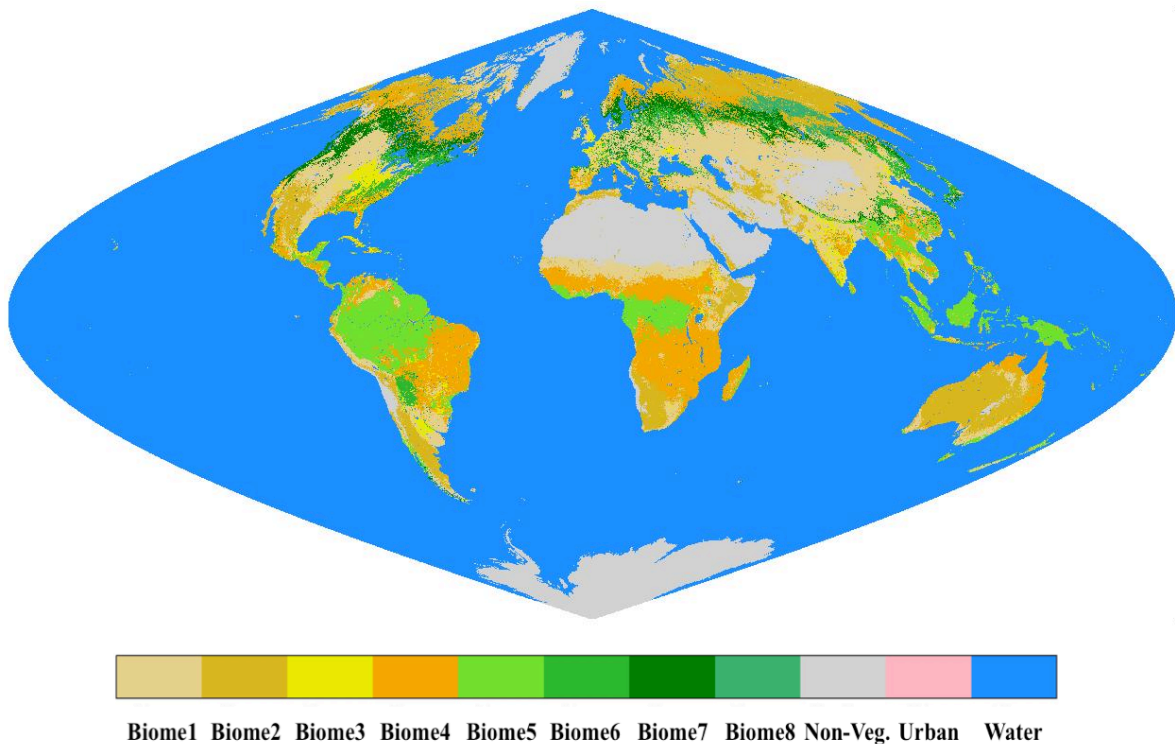


Figure 2-3. Global biome map input for VIIRS LAI/FPAR production. Global vegetation is stratified into eight canopy architectural types, or biomes. The eight biomes are (1) grasses and cereal crops, (2) shrubs, (3) broadleaf crops, (4) savannas, (5) evergreen broadleaf forests, (6) deciduous broadleaf forests, (7) evergreen needle leaf forests, (8) deciduous needle leaf forests.

Table 2-1. Canopy structural attributes of global land covers from the viewpoint of radiative transfer modeling.

	B1	B2	B3	B4	B5	B6	B7	B8
Horizontal heterogeneity	no	yes	variable	yes	yes	yes	yes	yes
Ground cover	100%	20-60%	10-100%	20-40%	> 70%	> 70%	> 70%	> 70%
Vertical heterogeneity (leaf optics and LAD*)	no	no	no	yes	yes	yes	yes	yes
Understory	no	no	no	grasses	yes	yes	yes	yes
Foliage dispersion	minimal clumping	random	regular	minimal clumping	clumped	clumped	severe clumping	severe clumping
Crown shadowing	no	not mutual	no	no	yes mutual	yes mutual	yes mutual	yes mutual
Brightness of canopy ground	medium	bright	dark	medium	dark	dark	dark	dark

*: Leaf Area Density

B1: Grasses and Cereal Crops, B2: Shrubs, B3: Broadleaf crops, B4: Savanna, B5: Evergreen Broadleaf forest, B6: Deciduous Broadleaf forest, B7: Evergreen Needleleaf forest, B8: Deciduous Needleleaf forest.

2.3. Radiation Transport in a Canopy

The solution of the RT equation for a vegetation medium is constructed from the solution of two sub-problems to which the notion of spectral invariance can be directly applied: (1) the black soil (BS) problem: the original illumination condition at the top of the canopy and the soil assumed to be absolutely absorbing; and (2) the soil (S) problem: there is no input energy from above, but a lambertian energy source is located at the bottom of the canopy. This decomposition technique is implemented in the LAI/FPAR operational algorithm. According to this approach, the spectral BRDF $\mathbf{r}_\lambda(\Omega)$ is approximated as below under given sun (Ω_0) and view (Ω) directions.

$$\mathbf{r}_\lambda(\Omega, \Omega_0) = w_{BS,\lambda} \cdot \mathbf{r}_{BS,\lambda}(\Omega_0) + w_{S,\lambda} \cdot \mathbf{t}_{S,\lambda} \cdot \frac{\rho_{eff}(\lambda)}{1 - \rho_{eff}(\lambda) \cdot \mathbf{r}_{S,\lambda}} \cdot \mathbf{t}_{BS,\lambda}(\Omega_0) \quad (\text{Equation 2-1})$$

Here $\mathbf{r}_{BS,\lambda}(\Omega_0)$ and $\mathbf{t}_{BS,\lambda}(\Omega_0)$ are directional hemispherical reflectance (DHR) and canopy transmittance for the black soil, and $\mathbf{r}_{S,\lambda}$ and $\mathbf{t}_{S,\lambda}$ are reflectance and transmittance resulting from an anisotropic source located underneath the canopy. The weight $w_{BS,\lambda}$ is the ratio of the BRDF for the black soil problem to $\mathbf{r}_{BS,\lambda}(\Omega_0)$, and $w_{S,\lambda}$ is the ratio of the canopy leaving radiance generated by anisotropic sources on the canopy bottom to $\mathbf{t}_{S,\lambda}$. The weights $w_{BS,\lambda}$ and $w_{S,\lambda}$ are functions of sun-view geometry, wavelength, and LAI. Note that $w_{BS,\lambda}$ and $w_{S,\lambda}$ are nearly wavelength independent. They are precomputed and stored in the LUT (Knyazikhin et al., 1999). The effective ground reflectance ρ_{eff} is the fraction of radiation reflected by the canopy ground. It depends on the radiative regime at the canopy bottom. However, its range of variations does not exceed the range of variations of the hemispherically integrated bidirectional factor of the ground surface, which is independent of vegetation (Knyazikhin et al., 1998a). Therefore, ρ_{eff} can be used as a parameter to characterize the ground reflection. The set of various patterns of effective ground reflectances at the spectral bands of given sensor is a static table of the algorithm, i.e., the element of the LUT. The present version of the LUT contains 29 patterns of ρ_{eff} ranging from bright to dark. They were taken from the soil reflectance model developed by Jacquemoud et al. (1992), with model inputs presented in Baret et al. (1993). While calculation of ground reflectances based on simplifying assumptions may be a weak point, the alternative, utilizing understory spectral databases (e.g. Kuusk et al., 2004; Peltoniemi et al., 2005) to characterize the background contribution for LAI retrievals for continental or global extents would be a significantly more demanding task as (a) there can be large variations in understory reflectances even within the same biome type, (b) variability of background reflectances is present at specific wavelengths across different regions, and (c) seasonal variations of background composition and their optical properties would comprise an added challenge.

Note that $\mathbf{r}_{BS,\lambda}(\Omega_0)$ and $\mathbf{r}_{S,\lambda}$ are not included in the LUT. Given canopy absorptance ($\mathbf{a}_{BS,\lambda}(\Omega_0)$ and $\mathbf{a}_{S,\lambda}$) and transmittance ($\mathbf{t}_{BS,\lambda}(\Omega_0)$ and $\mathbf{t}_{S,\lambda}$), they are evaluated via the law of energy conservation as

$$\mathbf{r}_{BS,\lambda} + \mathbf{t}_{BS,\lambda} + \mathbf{a}_{BS,\lambda} = 1 \quad (\text{Equation 2-2})$$

$$\mathbf{r}_{S,\lambda} + \mathbf{t}_{S,\lambda} + \mathbf{a}_{S,\lambda} = 1 \quad (\text{Equation 2-3})$$

This makes canopy reflectance sensitive to the within canopy radiation regime $\mathbf{t}_{BS,\lambda}(\Omega_0)$, $\mathbf{a}_{BS,\lambda}(\Omega_0)$, $\mathbf{t}_{S,\lambda}$ and $\mathbf{a}_{S,\lambda}$. The dependence of canopy absorptance on wavelength for the black soil problem (subscript $K = \text{“BS”}$) and S problem ($K = \text{“S”}$) can be derived (Knyazikhin et al., 1998a) as

$$\mathbf{a}_{K,\lambda} = \frac{1 - \omega(\lambda_0) \cdot p_K}{1 - \omega(\lambda) \cdot p_K} \cdot \frac{1 - \omega(\lambda)}{1 - \omega(\lambda_0)} \cdot \mathbf{a}_{K,\lambda_0} \quad (\text{Equation 2-4})$$

Here $\omega(\lambda)$ is the leaf albedo (leaf reflectance + leaf transmittance), also called single scattering albedo (SSA). It is a stable characteristic of green leaves, although its magnitude can vary with leaf age and species. In order to obtain accurate leaf albedos for the eight biome types, we obtained leaf spectra data from several sources. Mean leaf reflectance and transmittance values were calculated for the eight biome types at given spectral bands. We stored the mean albedo in the LUT. Variable p_K is a wavelength independent coefficient defined as (Knyazikhin et al., 1998a; Panferov et al., 2001)

$$p_K = 1 - \frac{\int_V \int_{4\pi} I_{K,BL}(r, \Omega) \cdot \sigma(r, \Omega) dr d\Omega}{\int_V \int_{4\pi} I_{K,WL}(r, \Omega) \cdot \sigma(r, \Omega) dr d\Omega} \quad (\text{Equation 2-5})$$

Where $I_{K,BS}$ and $I_{K,S}$ are solutions of the BS problem and S problem for black ($\omega = 0$, subscript BL) and white ($\omega = 1$, subscript WL) leaves, and σ is the extinction coefficient (dependent on vegetation types). V is a parallelepiped where vegetation canopies are located. Its height coincides with the height of plants and its horizontal dimension coincides with the size of the pixels. The coefficient p_K depends on canopy structure and V and is an element of the LUT. Because the horizontal dimension of V coincides with the size of pixel, p_K is a resolution dependent parameter. A precise derivation of Equation 2-4, and Equation 2-5 is given in (Knyazikhin et al., 1999). Validation of relationships presented in Equation 2-5 with field measurements is

presented in (Panferov et al., 2001). Similar relationships are also valid for canopy transmittance (Knyazikhin et al., 1998a; Huang et al., 2007). Thus, given canopy absorptance and transmittance for the BS problem and S problem at a reference wavelength λ_0 , one can evaluate these variables at any other wavelength λ . Therefore, we only store canopy absorptances \mathbf{a}_{K,λ_0} , transmittances \mathbf{t}_{K,λ_0} , the coefficients p_K , and leaf albedo, instead of $\mathbf{a}_{K,\lambda}$ and $\mathbf{t}_{K,\lambda}$ in the LUT. Reflectances $\mathbf{r}_{BS,\lambda}(\Omega_0)$ and $\mathbf{r}_{S,\lambda}$ can then be evaluated via the energy conservation law (Equation 2-2 and 2-3) and inserted into Equation 2-1. Note that BRDF is a product of $\mathbf{r}_{BS,\lambda}(\Omega_0)$ and $w_{BS,\lambda}$. Similar to Equation 2-1, the fraction of radiation absorbed by vegetation, $\mathbf{a}_\lambda(\Omega_0)$, at wavelength λ can be expressed as (Knyazikhin et al., 1998a)

$$\mathbf{a}_\lambda(\Omega_0) = \mathbf{a}_{BS,\lambda}(\Omega_0) + \mathbf{a}_{S,\lambda} \frac{\rho_{eff}(\lambda)}{1 - \rho_{eff}(\lambda) \cdot \mathbf{r}_{S,\lambda}} \mathbf{t}_{BS,\lambda}(\Omega_0) \quad (\text{Equation 2-6})$$

A value of FPAR can be explicitly evaluated as the integral of Equation 2-6 over photosynthetically active radiation (PAR, 400-700 nm) spectral region (Knyazikhin et al., 1998a). For the sake of brevity, all the details of theoretical formulation, mathematical evaluation and practical implementation of the LAI/FPAR algorithm are not provided here. Please check the MODIS Algorithm Theoretical Basis Documents (ATBD, Knyazikhin et al., 1999) for the details.

2.4. Theory of spectral invariants

Radiative transfer in vegetation canopies can be seen as a stochastic process, i.e. interacting photons can either be scattered or absorbed by a phytoelement (Stenberg et al., 2016). The probability of a scattering event, or SSA ($\omega(\lambda)$), depends on the wavelength and is a function of the leaf biochemical constitution. However, the probability that a photon will collide with elements again is determined by the structure of the canopy rather than the photon frequency or the optics of the canopy (Knyazikhin et al., 2005). Knyazikhin et al. (1998a) proposed the “ p -theory”, or “spectral invariants theory”, that describes the unique positive eigenvalue of the RT equation as the product of the leaf albedo and a wavelength-independent parameter (p , denoted as p_K hereinabove). This theory laid the foundation for the synergistic LUT-

based MODIS LAI/FPAR algorithm.

The spectral invariant principle is an important concept, because knowing the invariants of the canopy and the SSA of an average phytoelement at any wavelength makes it possible to reconstruct the radiation field of the canopy at any wavelength (Wang et al., 2003; Möttus and Stenberg, 2008). Introducing spectral invariant parameters permits decoupling of the structural and radiometric components of any optical sensor signal, which is the theoretical foundation of optimizing configurable parameters to achieve inter-sensor consistency in multi-sensor LAI/FPAR retrievals. Thus, the MODIS LAI/FPAR algorithm is applicable to any optical sensor by selecting the proper sensor-specific values of SSA. For MODIS LAI/FPAR algorithm, the 3D radiative transfer equation was used to generate the LUT – a set of tabulated BRF values (solution of the “BS-problem” and “S-problem”) as a function of SSA, for various LAI and sun-view geometries. To achieve accurate retrievals from a particular sensor like VIIRS, the simulated surface reflectances (i.e., BRFs derived from LUT) should be adjusted to be consistent with the expected range of the measured surface reflectances. The simulated surface reflectances are highly sensitive to leaf SSA for medium-to-high LAI and to soil reflectances for low LAI. The SSA is also a function of the spatial scale, therefore, it accounts for the variation in BRFs not only with sensor spectral characteristics but also with sensor spatial resolution (Ganguly et al., 2008a). Hence, a BRF can be computed for the sensor-specific resolution and spectral bands by adjusting the SSA.

2.5. Inverse problem and stabilized precision (Observation and model)

The inverse problem of retrieving LAI/FPAR from atmospherically corrected BRFs is formulated as follows. Let r_1, r_2, \dots, r_n be atmospherically corrected surface BRFs at n spectral bands. The surface reflectances are obtained by correcting at-sensor radiance for atmospheric effects. The correction technique introduces errors in the surface reflectance product. The operational LAI/FPAR algorithm treats spectral BRFs as independent random variables with finite variances σ_k^2 , $k=1,2,\dots,n$, and assumes that the deviations $\varepsilon_k = (r_k - m_k) / \sigma_k$ follow Gaussian distribution (Wang et al., 2001). Here m_k is the mathematical expectation of r_k , which approximates a true value. The random variable

$$\chi_{\sigma}^2[\mathbf{r} - \mathbf{m}] = \sum_{k=1}^n \varepsilon_k^2 = \sum_{k=1}^n \frac{(r_k - m_k)^2}{\sigma_k^2} \quad (\text{Equation 2-7})$$

characterizing the proximity of atmospherically corrected data $\mathbf{r} = (r_1, r_2, \dots, r_n)$ to the expected values $\mathbf{m} = (m_1, m_2, \dots, m_n)$ has a chi-square distribution. The inequality $\chi_{\sigma}^2 \leq n$ indicates good accuracy. We assume that the atmospheric correction algorithm provides spectral reflectance \mathbf{r} satisfying $\chi_{\sigma}^2 \leq n$ with a probability $1 - \alpha$. Dispersions $\sigma = (\sigma_1, \sigma_2, \dots, \sigma_n)$ are observation precisions, i.e., precision in the BRF product. The deviation of \mathbf{m} from a true vector is the measurement accuracy, or bias. The uncertainty is defined as the Root-Mean-Squared-Error (RMSE) between the estimated and true values, which depends on both accuracy and precision (Tan et al., 2005).

The operational algorithm compares measured spectral BRF, \mathbf{r} , with those evaluated from model-based entries, $\mathbf{r}_M = (r_{M,1}, r_{M,2}, \dots, r_{M,n})$, stored in the LUT. The model-based spectral BRF also has errors, which are characterized by values $\varepsilon_{M,k} = (r_{M,k} - m_{M,k}) / \sigma_{M,k}$. Dispersions $\sigma_M = (\sigma_{M,1}, \sigma_{M,2}, \dots, \sigma_{M,n})$ are model precisions, which are determined by the range of natural variation in biophysical parameters that are not accounted for by the model. Deviations of the model predictions, $m_{M,k}$, from true values characterize the model accuracy.

Both the observation and model precisions must be taken into account when comparing measured and modeled BRFs (Wang et al., 2001). Ignoring the model precision in the retrieval algorithm can cause a destabilization of the retrieval process. Wang et al. (2001) introduced a stabilized precision, $\delta = (\delta_1, \delta_2, \dots, \delta_n)$, which prevents the destabilization and minimizes the impact of model and observation precisions on LAI/FPAR retrievals. The stabilized precision is a function of σ_M and σ . The main LAI/FPAR algorithm uses the stabilized precision to select acceptable solutions, i.e., all canopy/soil parameters for which modeled, \mathbf{r}_M , and measured, \mathbf{r} , spectral BRFs agree within the stabilized precisions, i.e., $\chi_{\delta}^2[\mathbf{r} - \mathbf{r}_M] \leq n$. In the operational LAI/FPAR algorithm, relative stabilized precision (v_k), i.e., δ_k / r_k is used and MODIS specific v_k can be found in Table 2-4. The mean values of LAI/FPAR and their dispersions are reported as retrievals and their reliabilities. A detailed

mathematical justification of this procedure is presented in [Knyazikhin et al. \(1998a\)](#) and [Wang et al. \(2001\)](#).

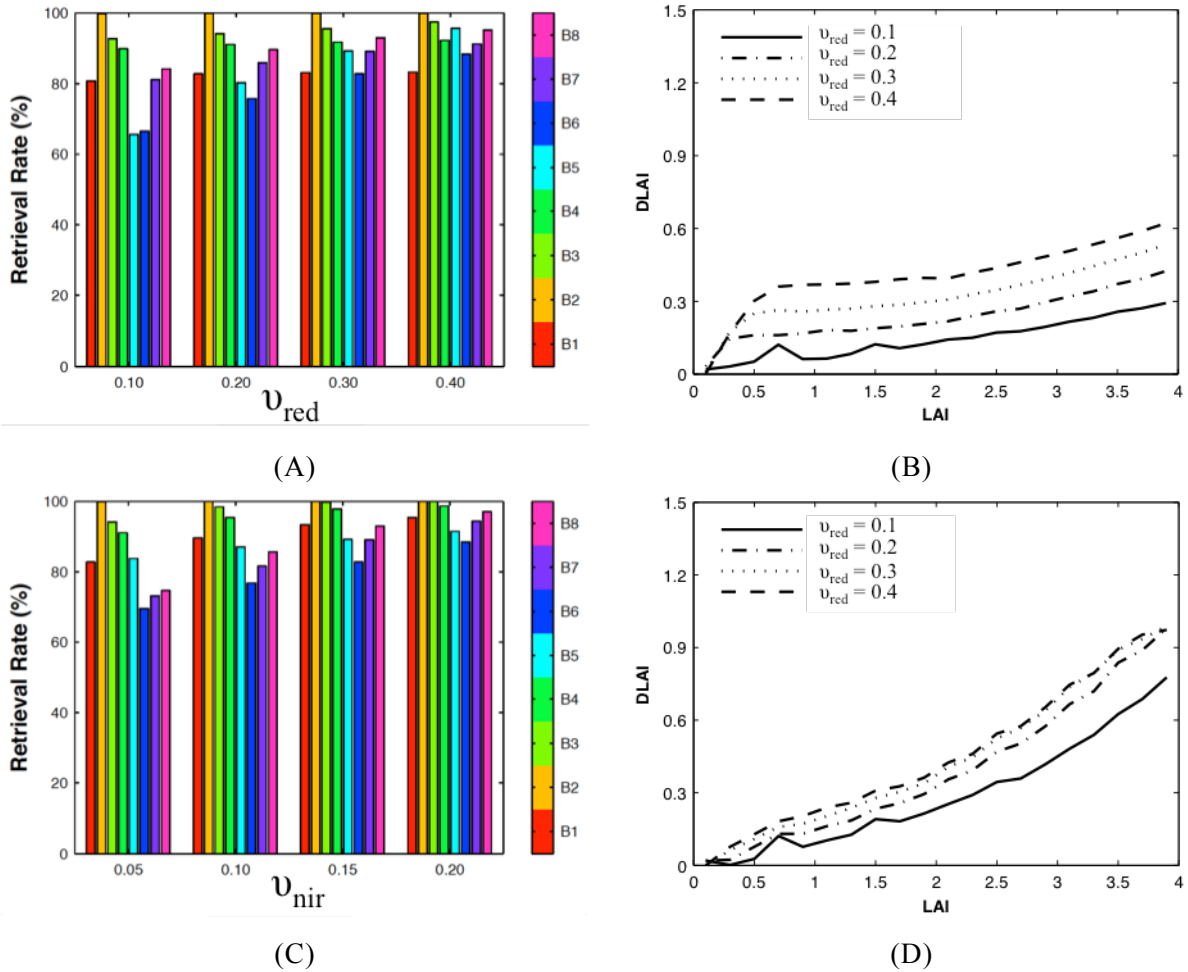


Figure 2-4. Dependence of the retrieval index (RI) on uncertainties, v , in measurements and simulations. (A) RI change under setting v_{nir} constant and v_{red} varying conditions. (B) Dispersion of LAI (DLAI) change as a function of LAI. Biome 3 (Broadleaf crops) case is given as an example. (C) and (D) are same as (A) and (B) but setting v_{nir} varying and v_{red} constant conditions.

Here, one experimental test is given to briefly illustrate the performance of the algorithm with respect to input/model uncertainties based on VIIRS surface reflectance data. To quantify the performance, the Retrieval Index (RI) is defined, which is the percentage of pixels for which the main algorithm produces retrievals ([Equation 2-8](#)). This index characterizes the spatial coverage of the best quality, high precision retrievals and not their accuracies.

$$RI = \frac{\text{number of main algorithm retrieved pixels}}{\text{number of total retrieved pixels}} \quad (\text{Equation 2-8})$$

Figure 2-4 demonstrates the dependence of the RI on v_k . The RI increases with an increase in v_k , but the reliability of retrievals (DLAI, dispersion of LAI) decreases. If v_k underestimates the true overall uncertainty, the algorithm fails to localize a solution, thus resulting in low values of RI. On the other hand, if v_k overestimates the algorithm admits a large number of solutions including non-physical solutions, thus resulting in high values of RI and DLAI. A critical value of v_k is one that optimally approximates the unknown true overall uncertainty. See Section 2.6 and 2.7 for VIIRS practice.

The LAI/FPAR operational algorithm uses BRF at two ($n=2$) spectral bands, red (band $k=1$) and NIR ($k=2$), to retrieve LAI/FPAR. Let $\mathbf{m}_T = (m_{T,1}, m_{T,2})$ and $\mathbf{m}_M = (m_{M,1}, m_{M,2})$ represent true values of the spectral BRF and expected values predicted by the model. It follows from the Minkowski inequality (Wang et al., 2001; Bronshtein et al., 2013) that

$$\chi_\delta[\mathbf{r} - \mathbf{r}_M] \leq \chi_\delta[\mathbf{r} - \mathbf{m}] + \chi_\delta[\mathbf{r}_M - \mathbf{m}_M] + \chi_\delta[\mathbf{m} - \mathbf{m}_M] \quad (\text{Equation 2-9})$$

This equation shows that χ_δ depends on how the modeled BRF differs from (a) “true” canopy BRF and (b) observed BRF. For example, the use of a very accurate model, i.e., $\mathbf{m}_T = \mathbf{m}_M$, maximizes the term $\chi_\delta[\mathbf{m} - \mathbf{m}_M]$. This may cause a “true” LAI to be outside of the set of acceptable solutions, i.e., it does not pass the comparison test. This term vanishes if one uses a model that tends to simulate the measurements, i.e., $\mathbf{m}_M = \mathbf{m}$. This however increases the contribution of the term $\chi_\delta[\mathbf{r}_M - \mathbf{m}_M]$. The calibration therefore is reduced to finding a surface reflectance model that optimally approximates the observed, \mathbf{m} , and true surface spectral BRF, \mathbf{m}_T .

The operational LAI/FPAR algorithm is based on the theory of canopy spectral invariants, which permits an accurate decoupling of the structural and radiometric components of modeled and/or measured spectral BRF (Knyazikhin et al., 1998a; Huang et al., 2007; Ganguly et al., 2008a; Knyazikhin et al., 2013). The structural component determines the BRF shape whereas the SSA controls its magnitude and accounts for the variation in BRF with sensor spatial resolution and spectral band composition (Ganguly et al.,

2008a). Thus the SSA and RSP that appear in the surface BRDF model are the adjustable parameters that control Equation 2-9 and consequently the performance of the LAI/FPAR retrieval technique.

2.6. Characteristics of Land Surface BRDFs

2.6.1. Spectral Characteristic

MODIS has 36 bands and VIIRS has 22 bands including a panchromatic day/night band (DNB) used for low light detection. A detailed comparison between MODIS and VIIRS spectral bands is documented in (Xiong et al., 2014). Figure 2-5 compares the Relative Spectral Response (RSR) of red and NIR bands between MODIS and VIIRS (available at <http://mcst.gsfc.nasa.gov/calibration/parameters> and <http://www.star.nesdis.noaa.gov/jpss/VIIRS.php> for MODIS and VIIRS, respectively). We notice that VIIRS has a NIR band RSR similar to MODIS, with almost the same bandwidth (0.039 vs. 0.036 μm) and slightly right-shifted center band (0.865 vs. 0.859 μm). However, the RSRs of MODIS and VIIRS red bands show obvious differences. VIIRS has broader bandwidth with the Full Width at Half Maximum (FWHM) ranging from 0.60 to 0.68 μm compared to MODIS's FWHM (0.62-0.67). The center red bands for VIIRS and MODIS are 0.639 and 0.645 μm , respectively.

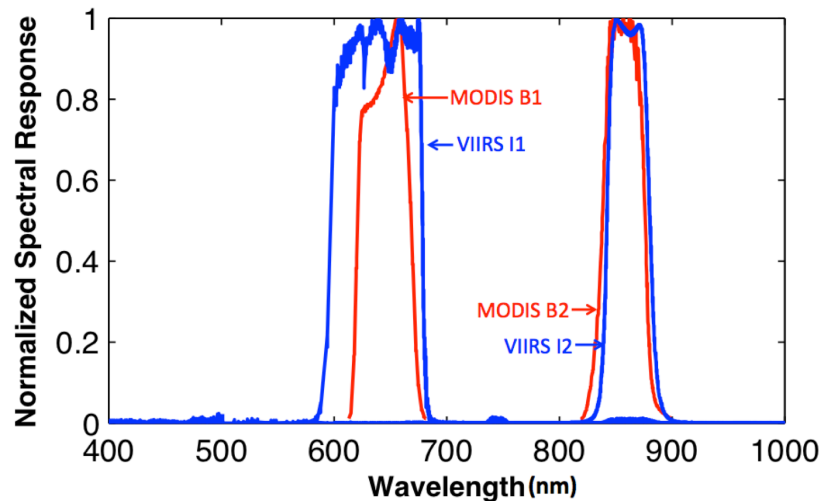


Figure 2-5. Normalized spectral response curves of visible infrared imaging radiometer suite (VIIRS) and moderate-resolution imaging spectroradiometer (MODIS) bands: Red (VIIRS-I1 and MODIS-B1), and near-infrared (VIIRS-I2 and MODIS-B2). Red and blue lines stand for MODIS and VIIRS bands, respectively.

2.6.2. Comparability of BRFs

To reduce computational cost of the optimization practice, VIIRS BRFs should be investigated first. The investigation aims: (a) to assure comparability between VIIRS and MODIS BRF precisions and (b) to quantify BRF differences between two sensors. We used the latest version of VIIRS (V1, VNP09GA) and Aqua MODIS (C6, MYD09GA) L2G surface reflectance data. Daily L2G surface reflectance data for the period July 4–11, 2015 are employed in this analysis. Global daily surface reflectance data are used. Eight select tiles (one per biome) are given as an example for each biome. The quality of both VIIRS and MODIS surface reflectance products are reported by QA. To achieve a precise measure of BRF precision and difference, the “best quality” observations are used, i.e., cloud free, snow free, aerosol low and average, adjacent cloud free and cirrus free observations. Discrepancy in sun-sensor geometry between the two datasets is minimized by only including minimally different observations (solar zenith angle difference $<2.5^\circ$, solar azimuth angle difference $<5^\circ$, sensor zenith angle difference $<5^\circ$, sensor azimuth angle difference $<5^\circ$).

Table 2-2. Precision comparison between MODIS MYD09GA and VIIRS VNP09GA. To minimize the impact of geometrical discrepancy between two sensors, strict angle difference threshold was applied. Only cloud free, shadow free, snow/ice free, low-average aerosol and cirrus free observations were sampled for this comparison purpose.

Biome	N	Difference of CV_{red}	Difference of CV_{nir}
Biome 1	6671803	0.031	0.010
Biome 2	7704215	0.007	0.001
Biome 3	974889	0.020	0.006
Biome 4	8084317	0.033	-0.002
Biome 5	1876055	0.003	-0.014
Biome 6	630298	0.059	0.006
Biome 7	479545	0.065	0.034
Biome 8	192863	0.030	0.021
All	26613985	0.025	0.009

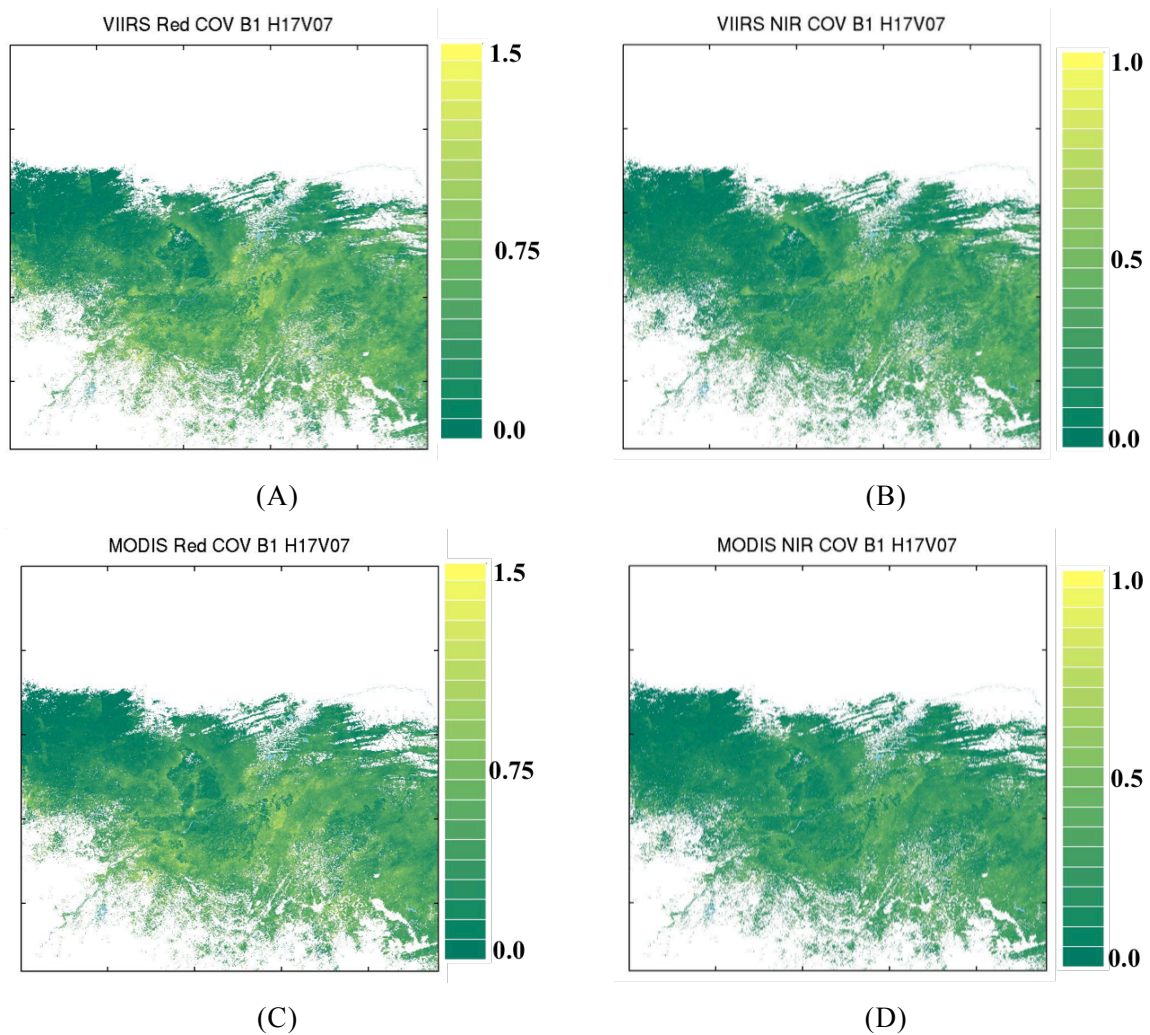


Figure 2-6. Spatial distribution of quantified precision (coefficient of variation, CV) of VIIRS and MODIS BRFs. This is an example of Biome 1 (Grasses/Cereal crops) dominant tile (H17V07). (A) and (B) display CVs of VIIRS BRF_{red} and BRF_{nir} , respectively. (C) and (D) are same as (A) and (B) but for MODIS.

If there are at least four daily surface reflectances of best quality during the 8-day period, then the precision comparison analysis was performed. Precision in surface reflectance from pixels with best quality data will therefore be due to incomplete atmospheric correction, while uncertainties in reflectances from pixels with non-best quality data will be due to improper cloud screening and instrumental anomalies (Tan et al., 2005). For the time being, it is assumed that the surface is unchanged over the measurement period of 8 days and that the solar and measurement geometry impact is minimal. The coefficient of variation per pixel is calculated from best quality daily surface reflectances during the 8-day period. As timing and number of selected best quality observations have an effect on precision comparison, only those pixels confirming order and number of best quality observations are used for this investigation. The precision of input BRFs can be characterized by the coefficient of

variation (e.g., [Hu et al., 2003](#); [Tan et al., 2005](#))

$$CV = \frac{S}{M} \quad (\text{Equation 2-10})$$

where M is the mean of measurements and S is the standard deviation of the measurement. Here, precision comparisons are made using CV 's rather than estimating relative stabilized precision of each sensor, as RSP is practically unmeasurable. [Table 2-2](#) summarizes the results. It suggests that overall BRF_{red} of VIIRS has relatively lower precision (2.5%) than MODIS while BRF_{nir} shows minimal difference (<1%). The difference of BRF_{red} precision (BRF_{nir}) depends on biome type and varies between 0.3% (-1.4%) and 6.5% (3.4%). [Figure 2-6](#) reveals strong spatial agreement between the two sensors and relatively lower and stable BRF input from NIR band than red spectral band. These generally comparable precision values justifies setting the relative stabilized precision to that used to generate C6 MODIS LAI/FPAR product (See [Table 2-4](#)). Also this result supports the relatively uncertain red band BRF reported in (<http://modis-sr.ltdri.org/pages/validation.html>).

Unlike the evaluation of precision, all available daily VIIRS/MODIS observations with best quality are used to quantify BRF differences. [Table 2-3](#) summarizes the absolute and relative differences. The magnitude of difference varies by biome type. Biome 2 (Shrublands) has most comparable BRFs whereas Biome 5 (Evergreen broadleaf forests) shows the largest relative discrepancy. Generally VIIRS shows relatively lower BRF_{red} (-13.9% ~ -2.9%) and higher BRF_{nir} (1.2% ~ 4.9%) indicating possible overestimation of LAI/FPAR and declining performance of the main algorithm without sensor-specific parametric optimization ([Figure 2-7](#)). Indeed, global VIIRS retrievals without parametric optimization reveal clear LAI/FPAR overestimation and reduced performance across all biome types ([Figure 2-10 and Table 2-5](#)). These results justify SSA based VIIRS specific parametric optimization.

Table 2-3. Comparison between MODIS MYD09GA and VIIRS VNP09GA. To minimize the impact of geometrical discrepancy between two sensors, strict angle difference threshold was applied. Only cloud free, shadow free, snow/ice free, low-average aerosol and cirrus free observations were sampled for this comparison purpose.

Biome	N	$\Delta\text{BRF}_{\text{red}}$	$\Delta\text{BRF}_{\text{NIR}}$	$\Delta\text{BRF}_{\text{red}}\%$	$\Delta\text{BRF}_{\text{NIR}}\%$
1	6671803	-0.0036	0.0096	-3.09	3.30
2	7704215	-0.0033	0.0088	-2.91	3.29
3	974889	-0.0045	0.0132	-6.13	3.84
4	8084317	-0.0035	0.0076	-5.64	3.06
5	1876055	-0.0039	0.0158	-11.22	4.91
6	630298	-0.0036	0.0102	-11.21	3.43
7	479545	-0.0032	0.0031	-9.89	1.44
8	192863	-0.0041	0.0027	-13.89	1.17

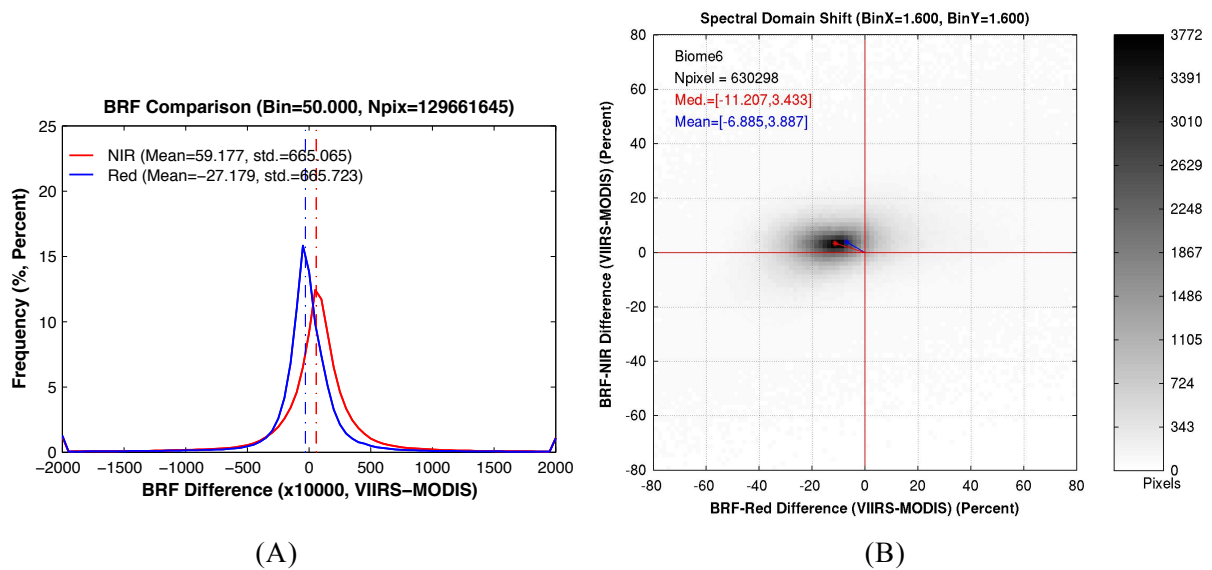


Figure 2-7. (A) Histogram of absolute BRF difference at red and NIR band across all biomes. Positive difference means VIIRS BRF is higher than MODIS one, vice versa. (B) Relative BRF difference at red and NIR band are plotted in spectral domain. Obvious left- and up-ward spectral shift is observed. For this comparison, the latest version of VIIRS (VNP09GA) and MODIS (MYD09GA) L2G daily surface reflectance data sets are used (July 4–11, 2015). And strict quality control and minimal sun-view geometry difference are applied to use only best quality observations.

2.7. Solving the optimization problem

The performance metrics of the LAI/FPAR operational algorithm include (1) the retrieval index (RI, Equation 2-8), (2) RMSE between a reference LAI value and LAI value retrieved by the main algorithm, and (3) proximity of LAI histograms obtained from the main algorithm and reference data. The retrieval index is the percentage of pixels for which the main algorithm produces a result. This index characterizes the spatial coverage of the best quality, high precision retrievals and not their accuracies. The RMSE and proximity between main algorithm retrievals and reference data

characterize the product accuracy. To quantify the proximity of LAI histograms between retrievals and reference datasets, a complementary decision rule, which is checking for Accuracy, Precision and Uncertainty (APU) over possible LAI ranges (Figure 2-8B, an example for biome 6), is implemented to mediate unexpected bias in addition to RI & RMSE metrics (Figure 2-8A). Furthermore, an algorithm match index (AMI) that accounts for the rate of retrieved pixels via the same algorithm path (i.e., both retrieval and reference are from the main algorithm with or without saturation) is implemented because increasing mismatch magnifies disagreement (Myneni et al., 2002; Yan et al., 2016a).

$$AMI = \frac{\text{number of retrieved pixels via same algorithm path}}{\text{number of total retrieved pixels}} \quad (\text{Equation 2-11})$$

There are at least three reasons justifying the use of MODIS C6 LAI/FPAR retrievals as reference data: (1) ground LAI/FPAR measurements are spatiotemporally limited to solve the optimization problem, (2) MODIS operational algorithm is well-optimized for C6 BRF inputs, and (3) the ultimate goal is assuring consistency between VIIRS and MODIS. Thus the validated global MODIS C6 LAI/FPAR product with good quality pixel BRFs generated by the main algorithm during the compositing period between 4 and 11 July 2015 is used as the reference data set. The performance metrics are a function of the SSA at red and NIR spectral bands. The optimization procedure therefore can be formulated as follows: find a combination of SSAs at red, ω_{red} , and NIR, ω_{nir} , spectral bands which (a) maximizes the RI; (b) minimizes the RMSE and (c) also minimizes the disagreement between LAI histograms generated by the main algorithm VIIRS retrievals and MODIS C6 LAI product. This procedure is illustrated in Figure 2-8. First, we calculated the RI and RMSE as a function of ω_{red} and ω_{nir} . Second, we separated a subset of first 10 best pairs (ω_{red} , ω_{nir}) rather than using a pre-set threshold because RI and RMSE vary significantly by biome type and sample datasets. Finally, we selected a pair (ω_{red} , ω_{nir}) from this subset for which disagreement between LAI histograms obtained from the main algorithm retrievals and MODIS C6 LAI was minimized.

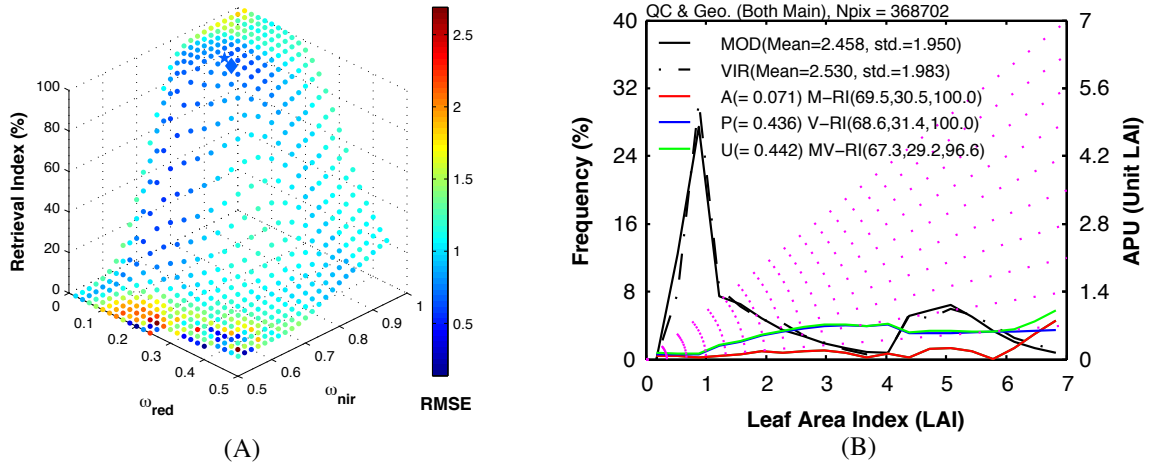


Figure 2-8. (A) The difference (RMSE) between MODIS and VIIRS LAI values and the Retrieval Index (RI) as a function of the single scattering albedo at red (ω_{red}) and NIR (ω_{nir}) spectral bands. Each circle represents possible combination of both parameters. Diamond and star markers represent derivation of MODIS based and optimally selected parametric combinations, respectively. (B) LAI histograms of MODIS and VIIRS with quantified APU (Accuracy, Precision and Uncertainty) statistics. Since considering only RI and RMSE introduces biased optimized single scattering albedo depending on given sample characteristics, we attempted to take account of APU measures. The algorithm match index (AMI) is additionally used to quantify their agreement. Here, three numbers following MV-RI represents rates of matched main algorithm path under without saturation (67.3%), saturation (29.2%) and both (96.6%) conditions. In this example, AMI is 96.6% suggesting that only 3.4% of the pair (retrieval and reference) pixels are retrieved with different condition.

Table 2-4 shows values of SSA at red and NIR spectral bands used in the MODIS C6 operational algorithm and adjusted for VIIRS data. These values optimally approximate the observed and true surface spectral BRF values. The biome-specific SSA show lower values at red than the heritage case of MODIS and higher values at near-infrared band. These changes are in agreement with our BRF evaluation results presented in Section 2.6.2. Figure 2-9 shows an example of model-based LUT entries used in the MODIS C6 operational algorithm and adjusted for the VIIRS data. For a given LAI and soil pattern, the VIIRS LUT generates slightly lower BRF_{red} and higher BRF_{nir} values compared to those for MODIS MYD09GA BRF data. The main algorithm accumulates acceptable solutions, i.e., all canopy/soil parameters for which observed spectral BRF, \mathbf{r} , agree with LUT entries, \mathbf{r}_M , within the stabilized precisions, i.e., $\chi^2[\mathbf{r} - \mathbf{r}_M] \leq 2$. Figure 2-8B shows the distribution of LAI in the NIR vs red spectral plane. The retrieval domain is a set of points on the spectral plane for which the model-based main algorithm retrieves at least one acceptable solution. In the case of dense canopies, the reflectances saturate, and therefore are weakly sensitive to changes in canopy properties. The saturated reflectances are shown as a green-to-yellow subset in the retrieval domain. The configuration of the retrieval domain is

controlled by the stabilized precision and single scattering albedo values at red and NIR spectral bands.

Table 2-4. The single scattering albedos (ω) and relative stabilized precision (ν) for red and near-infrared wavelengths from MODIS LUT heritage and adjusted VIIRS LUT

Biome	MODIS LUT based ν		MODIS LUT based ω		Adjusted VIIRS LUT ω			
	ν_{red}	ν_{nir}	ω_{red}	ω_{nir}	ω_{red}	ω_{nir}	$\Delta\omega_{red}$	$\Delta\omega_{nir}$
1	0.2	0.05	0.18	0.88	0.14	0.89	-0.04	+0.01
2	0.2	0.05	0.16	0.84	0.13	0.86	-0.03	+0.02
3	0.2	0.05	0.10	0.94	0.05	0.95	-0.05	+0.01
4	0.2	0.05	0.14	0.88	0.09	0.89	-0.05	+0.01
5	0.3	0.15	0.151	0.910	0.10	0.93	-0.051	+0.02
6	0.3	0.15	0.14	0.84	0.12	0.85	-0.02	+0.01
7	0.3	0.15	0.14	0.70	0.11	0.70	-0.03	0
8	0.3	0.15	0.14	0.70	0.11	0.70	-0.03	0

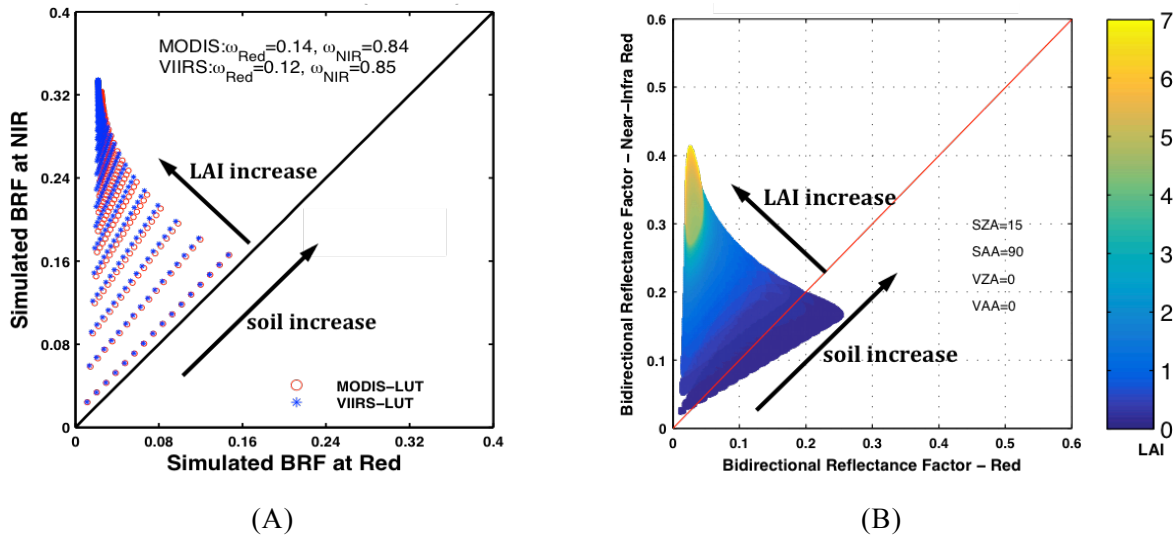


Figure 2-9. (A) Look-Up-Table (LUT) entries on the Near-infrared (NIR) vs. red spectral plane adjusted for MODIS MYD09GA (circles) and VIIRS VNP09GA (asterisk) BRF data. (B) Retrieval domain of the algorithm calibrated for VIIRS BRF data. The main LAI algorithm can retrieve a LAI value only if the observed pair (BRF_{red}, BRF_{nir}) of VIIRS BRF at red and NIR spectral bands falls within the retrieval domain. Color bar shows returned LAI value per unit red vs NIR spectral plane. The LUT entries and retrieval domain are for broadleaf forests (Biome 6), solar zenith angle between 22.5° to 37.5° , view zenith angle between 0° to 8.5° and the relative azimuth angle between 0° to 25° .

Figure 2-10 shows a comparison of Aqua MODIS C6 and VIIRS LAI/FPAR without (cyan) and with (magenta) parametric optimization generated by the main algorithm during the compositing period between 4 and 11 July 2015. Note that the results shown in this Section are based on the data used for optimization – thus, further consistency evaluation is required. The majority of the retrievals without adjustment tend to overestimate LAI (0.15) and FPAR (0.03) as expected from BRF comparisons

(See [Section 2.6.2](#)). In particular, forest biomes (biome 5 to 8) exhibit larger LAI overestimation (0.17 – 0.43) whereas non-forest biomes (biome 1 to 4) show relatively higher FPAR disparity (0.03 – 0.04). Overall difference between VIIRS and C6 LAI values has been reduced from 0.43 to 0.08 LAI units after algorithm calibration for VIIRS data ([Table 2-5](#)). Parametric adjustment also reconciles the gap between C6 and VIIRS FPAR values from 0.03 units to 0.005 FPAR units. The results demonstrate that the implemented optimization method and parameter selection were successful in reducing the bias between reference and VIIRS retrievals and also help closely track the frequency distribution of MODIS C6 LAI/FPAR data ([Figure 2-11](#)).

Table 2-5. Comparison between VIIRS and MODIS LAI/FPAR retrievals with MODIS-LUT and Optimized-LUT for VIIRS. Bias is calculated by subtracting MODIS retrieval from VIIRS’.

Biome	N	LAI				FPAR			
		MODIS-LUT		Optimized-LUT		MODIS-LUT		Optimized-LUT	
		Bias	RMSE	Bias	RMSE	Bias	RMSE	Bias	RMSE
1	6671803	0.109	0.406	-0.003	0.338	0.028	0.091	0.005	0.083
2	7704215	0.099	0.312	0.008	0.240	0.030	0.082	0.007	0.072
3	974889	0.166	0.497	0.011	0.399	0.033	0.110	0.003	0.101
4	8084317	0.193	0.519	0.034	0.424	0.038	0.105	0.008	0.094
5	1876055	0.205	0.702	0.041	0.659	0.003	0.089	-0.003	0.090
6	630298	0.174	0.613	-0.033	0.537	0.017	0.065	-0.001	0.059
7	479545	0.239	0.871	-0.035	0.800	0.025	0.137	-0.003	0.133
8	192863	0.427	0.858	0.084	0.747	0.026	0.078	0.001	0.074
Total	26613985	0.146	0.472	0.014	0.398	0.030	0.094	0.005	0.086

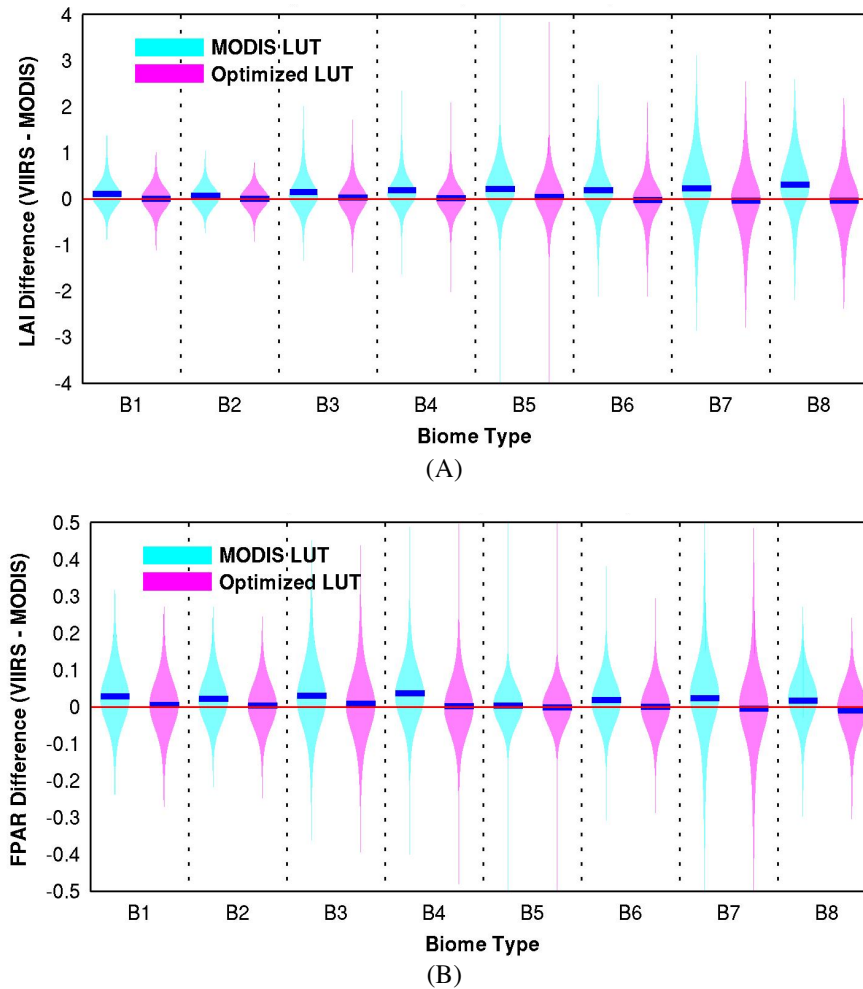


Figure 2-10. (A) LAI difference (VIIRS LAI – MODIS LAI) distributions of before (MODIS LUT) and after optimization (Optimized LUT). Global surface reflectance and its retrieval during a compositing period (July 4 to July 11) in 2015 are used in this analysis. Cyan and magenta violin plots represent distribution of differences under MODIS LUT and newly optimized VIIRS own LUT. A blue line in each violin plot stands for mean value of differences. (B) Same as (A) but for FPAR.

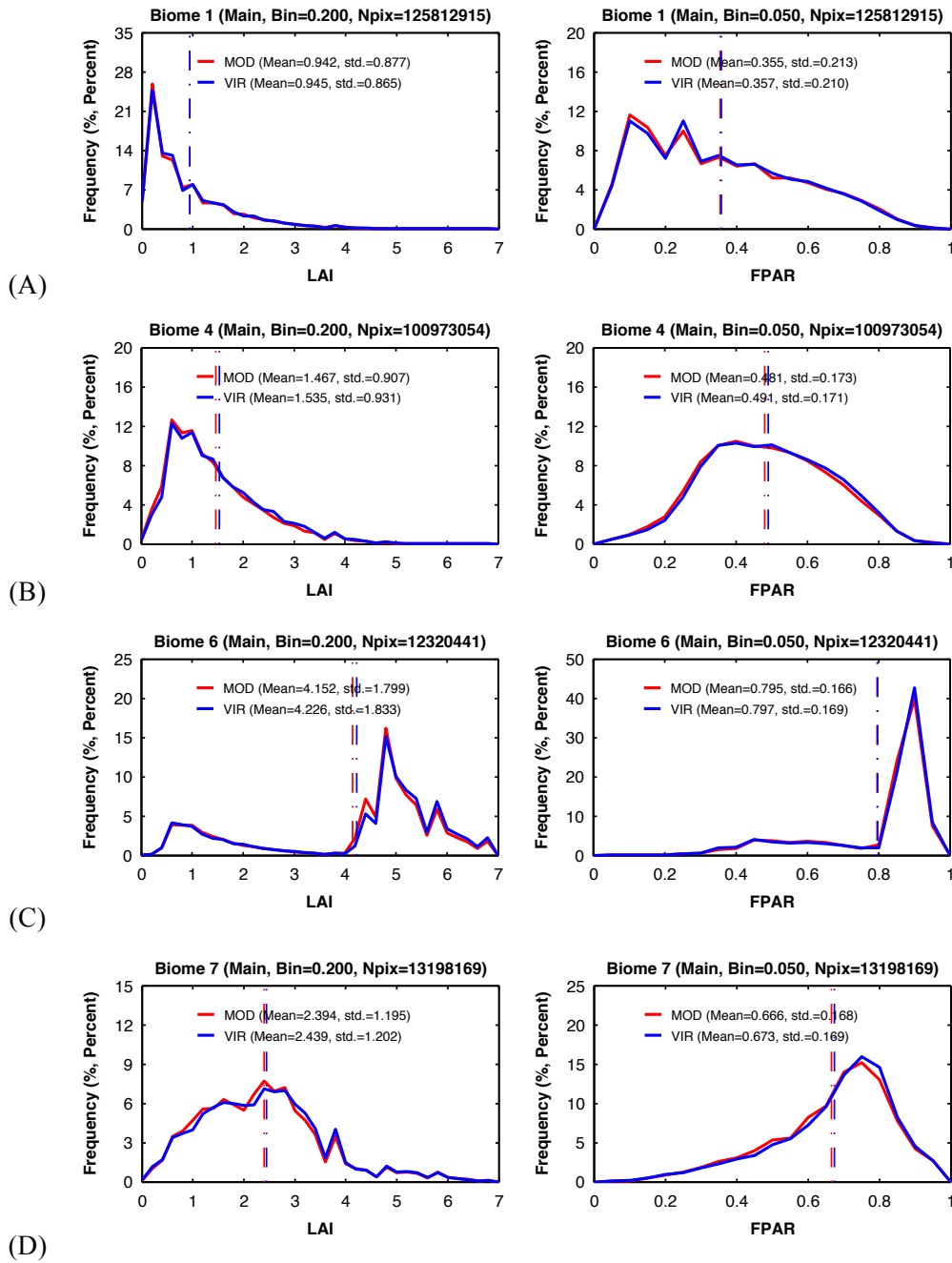


Figure 2-11. Histogram of globally generated VIIRS and MODIS LAI/FPAR retrievals. The retrievals are from the latest version of L2G VNP09GA and MYD09GA data in July 2015 (DOY185-192) and optimized LUTs for each sensor. Observations satisfying best quality and minimal geometry difference requirements are considered for retrievals. Only main algorithm under both unsaturation and saturation conditions are used. Red and blue solid lines represent Aqua MODIS and VIIRS retrievals, respectively. And dotted lines show mean value of derivations. Here, four biomes are listed as examples. (A) Biome1: Grasses/Cereal crops, (B) B4: Savanna, (C) B6: Deciduous Broadleaf forest and (D) B7: Evergreen Needleleaf forest.

Not surprisingly, the adjustment procedure also results in improving the spatial coverage of the VIIRS product, i.e. increased RI. Figure 2-12 shows the before- and after-optimization distribution of algorithm path for VIIRS and Aqua MODIS input

BRFs as a function of biome type. The case before-adjustment shows comparable RIs over non-forest biomes (less by 0.5-1.7%) but significantly less RIs in forest biomes (less by 6.0-12.0%). The optimized VIIRS LUT yields equivalent rates (within $\pm 1.3\%$ RI difference) of main algorithm retrievals over all biomes. The saturation frequency and dispersion of the retrieved LAI distribution are two elements by which the quality of the retrieval can be assessed. The accuracy of the retrieval decreases under conditions of saturation, that is, the reflectance data contain less accurate information about the surface (Knyazikhin et al., 1998a). Therefore, the saturation frequency and the threshold LAI value of saturation on a biome-by-biome basis are important criteria for assessing the accuracy of the retrievals. The probability of retrieving the highest quality LAI/FPAR values (i.e., main algorithm without saturation condition) is higher than 90% for non-forest biomes. Broadleaf forests (biome 5 & 6) represent dense canopies, thus the majority of the LAI/FPAR values are retrieved under the condition of saturation and therefore have moderate quality.

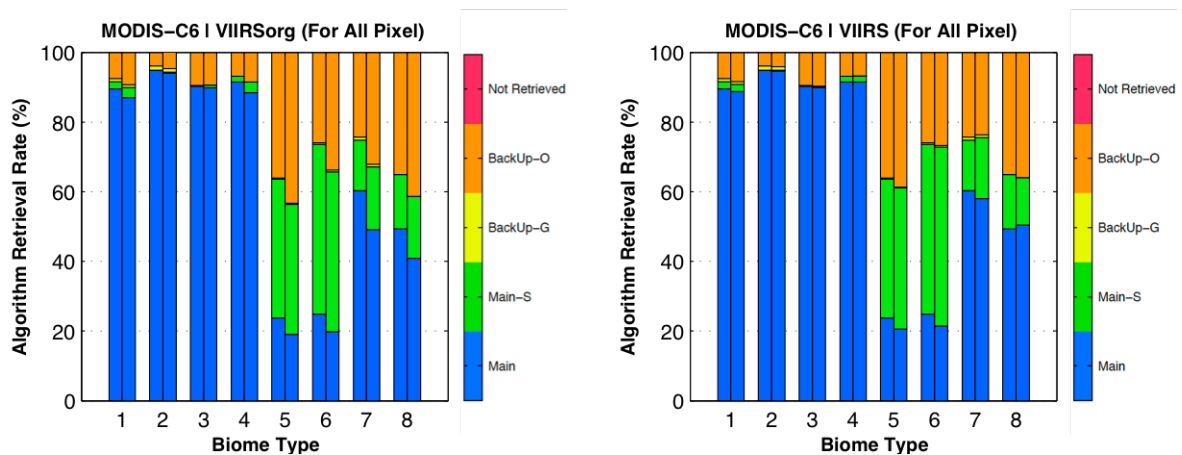


Figure 2-12. Algorithm retrieval rate (%) of MODIS C6 (left bars) and VIIRS (right bars) by biome types. (A) Before adjustment and (B) after adjustment. Retrievals during a compositing period (July 4 to July 11) in 2015 are used. Algorithm retrieval rate is defined as the ratio of the number of pixels with LAI and FPAR retrieved by each algorithm path to the total number of retrievals by both the main and backup algorithms. Legends: Main – Main algorithm was executed; Main-S - Main algorithm was executed. Saturation; BackUp-G - View/sun zenith angle too low. Backup retrievals; BackUp-O - Main algorithm fails. Backup retrievals; Not Retrieved - not executed because BRF is not available.

2.8. Backup Algorithm

If there are no candidate biome/canopy models that can pass the comparison test for a given pixel, a backup algorithm is triggered to estimate LAI and FPAR using the Normalized Difference Vegetation Index (NDVI). This backup algorithm requires a

land cover classification that is compatible with the RT model used in their derivation. Backup algorithm uses regression curves to estimate LAI and FPAR values, namely,

$$LAI = f_1(NDVI), FPAR = f_2(NDVI) \quad (\text{Equation 2-12})$$

Here, f_1 and f_2 are biome dependent regression curves which are derived as follows. Based on finalized main algorithm LUT, VIIRS LAI/FPAR backup LUT using LAI-NDVI or NDVI-FPAR empirical relations have been developed as: (Step 1) Collect all main retrievals from global LAI retrievals and their corresponding NDVI values. (Step 2) Obtain mean NDVI of binned LAI intervals (300 intervals for the LAI range 0-7). (Step 3) Regress LAI-NDVI relation and obtain NDVI-LAI LUT (2nd order exponential and spline fitting for LAI-NDVI and FPAR-NDVI respectively). (Step 4) Extract LAI, FPAR and NDVI with unequal step used for MODIS algorithm. This allows more frequent sampling of parts of the LAI-NDVI curve, where shape of the curve changes rapidly. [Figure 2-13](#) shows an example of VIIRS LUT preparation for biome 1 (Grasses/Cereal crops). The empirically derived regression curves of NDVI-LAI and NDVI-FPAR for all 8 biomes can be found in [Figure 2-14](#). The backup algorithm consists of a direct FPAR and LAI retrieval using the pixels biome-class and the current pixel's NDVI value as the search keys. In the LUT itself, there are 20 unequal-interval LUT records per biome class. The backup LUT is summarized in [Table 2-6](#).

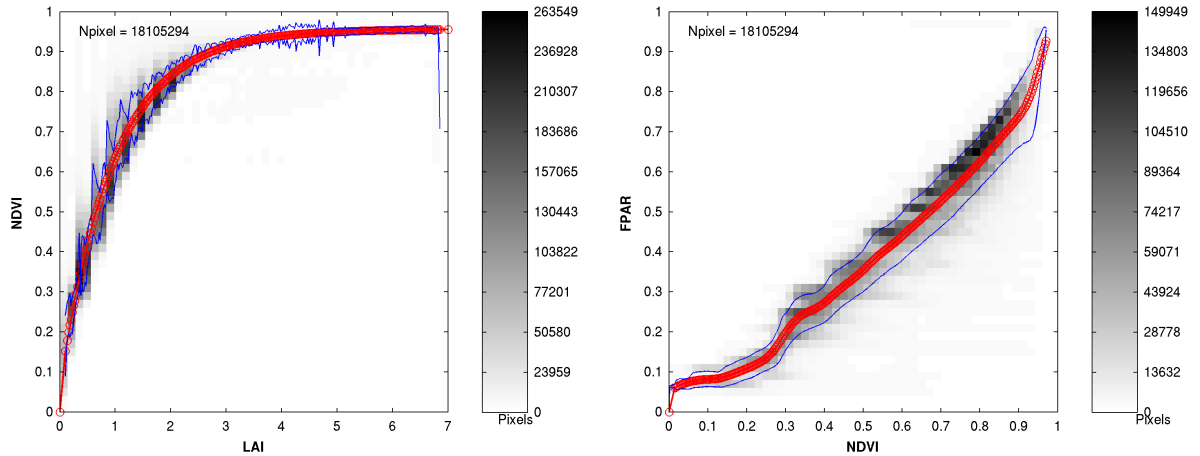


Figure 2-13. Schematic illustration of the backup algorithm. (A) Observed VIIRS LAI-NDVI relationship from main algorithm retrievals. Background density plot summarizes globally collected main algorithm based LAI-NDVI scatters. Red and blue lines represent sets of mean and standard deviation ($\pm 1\text{std}$) of NDVIs within binned LAI interval, respectively. (B) Same as (A) but for FPAR-NDVI. Biome 3 (Broadleaf crops) case is introduced as an example.

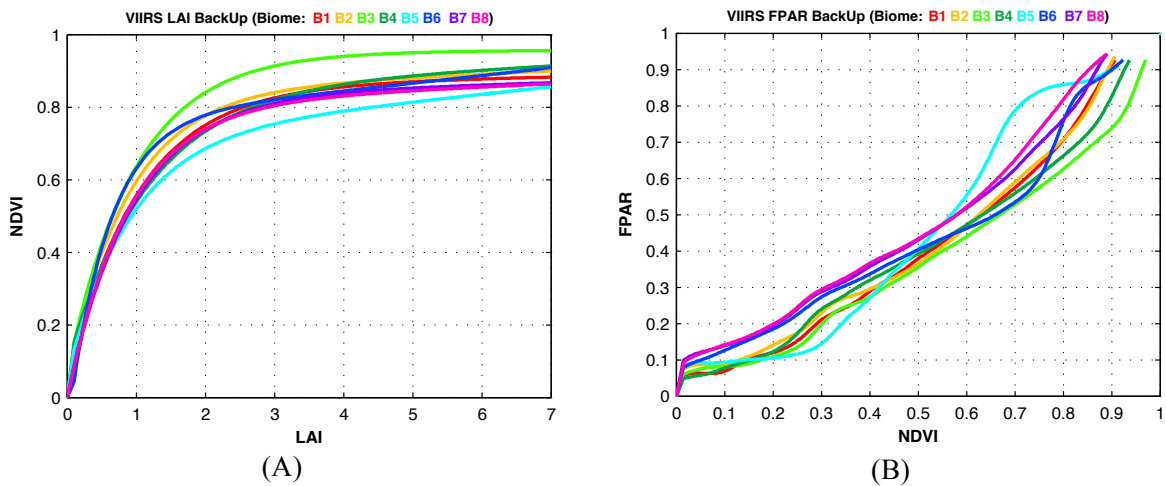


Figure 2-14. Empirically derived regression curves of NDVI-LAI (A) and NDVI-FPAR (B) for 8 biomes. The regressed relationships are based on global main algorithm retrievals. Parametrically optimized main algorithm LUT and VIIRS V1 VNP09GA are used to retrieve the global retrievals data sets. Colored lines represent each biome type, i.e., B1: Grasses/Cereal crops, B2: Shrubs, B3: Broadleaf crops, B4: Savanna, B5: Evergreen Broadleaf forest, B6: Deciduous Broadleaf forest, B7: Evergreen Needleleaf forest, B8: Deciduous Needleleaf forest.

Table 2-6. NDVI and corresponding values of LAI and FPAR in VIIRS V1 back-up LUTs

Biome1			Biome2			Biome3			Biome4			Biome5			Biome6			Biome7			Biome8		
NDVI	LAI	FPAR																					
0.000	0.000	0.000	0.000	0.000	0.000	0.000	0.000	0.000	0.000	0.000	0.000	0.000	0.000	0.000	0.000	0.000	0.000	0.000	0.000	0.000	0.000	0.000	0.000
0.120	0.100	0.082	0.139	0.100	0.104	0.151	0.100	0.090	0.153	0.100	0.099	0.095	0.050	0.093	0.045	0.100	0.097	0.088	0.100	0.134	0.086	0.100	0.135
0.361	0.500	0.252	0.398	0.500	0.294	0.422	0.500	0.292	0.360	0.500	0.288	0.129	0.100	0.098	0.411	0.500	0.344	0.343	0.500	0.313	0.351	0.500	0.327
0.524	0.900	0.401	0.564	0.900	0.426	0.602	0.900	0.441	0.508	0.900	0.397	0.162	0.150	0.101	0.600	0.900	0.462	0.512	0.900	0.440	0.522	0.900	0.451
0.635	1.300	0.505	0.671	1.300	0.555	0.720	1.300	0.546	0.614	1.300	0.483	0.193	0.200	0.104	0.699	1.300	0.533	0.624	1.300	0.541	0.631	1.300	0.557
0.676	1.500	0.547	0.709	1.500	0.601	0.764	1.500	0.589	0.655	1.500	0.518	0.234	0.270	0.112	0.730	1.500	0.566	0.665	1.500	0.583	0.670	1.500	0.608
0.710	1.700	0.586	0.740	1.700	0.637	0.799	1.700	0.625	0.690	1.700	0.549	0.287	0.370	0.133	0.753	1.700	0.607	0.699	1.700	0.624	0.702	1.700	0.654
0.738	1.900	0.620	0.765	1.900	0.666	0.828	1.900	0.656	0.719	1.900	0.577	0.348	0.500	0.209	0.770	1.900	0.655	0.726	1.900	0.662	0.728	1.900	0.696
0.761	2.100	0.650	0.786	2.100	0.689	0.851	2.100	0.683	0.745	2.100	0.602	0.409	0.650	0.283	0.784	2.100	0.702	0.749	2.100	0.693	0.748	2.100	0.730
0.780	2.300	0.677	0.802	2.300	0.710	0.870	2.300	0.704	0.766	2.300	0.625	0.448	0.760	0.340	0.795	2.300	0.740	0.767	2.300	0.718	0.765	2.300	0.758
0.796	2.500	0.700	0.816	2.500	0.729	0.886	2.500	0.722	0.785	2.500	0.645	0.497	0.920	0.402	0.804	2.500	0.769	0.782	2.500	0.738	0.779	2.500	0.781
0.809	2.700	0.722	0.827	2.700	0.746	0.899	2.700	0.737	0.800	2.700	0.663	0.542	1.090	0.462	0.811	2.700	0.790	0.795	2.700	0.755	0.790	2.700	0.800
0.820	2.900	0.742	0.836	2.900	0.762	0.909	2.900	0.751	0.814	2.900	0.678	0.589	1.310	0.534	0.817	2.900	0.807	0.805	2.900	0.770	0.800	2.900	0.816
0.830	3.100	0.760	0.844	3.100	0.776	0.917	3.100	0.765	0.826	3.100	0.691	0.648	1.680	0.663	0.823	3.100	0.819	0.814	3.100	0.783	0.808	3.100	0.830
0.837	3.300	0.776	0.850	3.300	0.790	0.924	3.300	0.779	0.836	3.300	0.703	0.735	2.640	0.827	0.828	3.300	0.829	0.821	3.300	0.795	0.814	3.300	0.841
0.844	3.500	0.790	0.856	3.500	0.802	0.930	3.500	0.792	0.845	3.500	0.715	0.775	3.560	0.851	0.833	3.500	0.837	0.827	3.500	0.806	0.820	3.500	0.851
0.849	3.700	0.802	0.860	3.700	0.813	0.935	3.700	0.805	0.853	3.700	0.726	0.808	4.760	0.860	0.838	3.700	0.843	0.832	3.700	0.815	0.824	3.700	0.858
0.854	3.900	0.812	0.864	3.900	0.824	0.938	3.900	0.816	0.860	3.900	0.737	0.825	5.520	0.864	0.842	3.900	0.848	0.837	3.900	0.824	0.829	3.900	0.865
0.858	4.100	0.821	0.868	4.100	0.833	0.941	4.100	0.826	0.866	4.100	0.747	0.835	6.000	0.868	0.847	4.100	0.853	0.840	4.100	0.832	0.832	4.100	0.871
1.000	7.000	1.000	1.000	7.000	1.000	1.000	7.000	1.000	1.000	7.000	1.000	1.000	7.000	1.000	1.000	7.000	1.000	1.000	7.000	1.000	1.000	7.000	1.000

B1: Grasses/Cereal crops, B2: Shrubs, B3: Broadleaf crops, B4: Savanna,
 B5: Evergreen Broadleaf forest, B6: Deciduous Broadleaf forest, B7: Evergreen Needleleaf forest, B8: Deciduous Needleleaf forest.

3. Product

3.1. Product Description

The VIIRS land product suite is composed of three different levels (swath product – derived geophysical variables at the same resolution and Level-1 source data), Level 3 (gridded variables in derived spatial and/or resolutions), and Level 4 (model output or results from analyses of lower data sets. Currently, the LAI/FPAR data set is defined as Level 4 processing explicitly modeled photon transfer in vegetation medium is a fundamental operational algorithm. The operational VIIRS LAI/FPAR algorithm currently uses (a) VNP09GA L2G 500m surface reflectance data (red and NIR bands, i.e. with given geometry and QA information and (b) an 8-biome L3 classification map (MCDLCHKM, 500m). Details of input data are given in [Figure 3.2](#). The algorithm generates two Level 4 products at the Land SIPS ([Figure 3.2](#) and [Table 3-1](#) for details). The 8-day composite LAI, FPAR and corresponding SCF_QC layer in product) are shown in [Figure 3-1](#) as an example. The corresponding input BRFs and retrieved LAI/FPAR also can be found in [Figure 3-1](#).

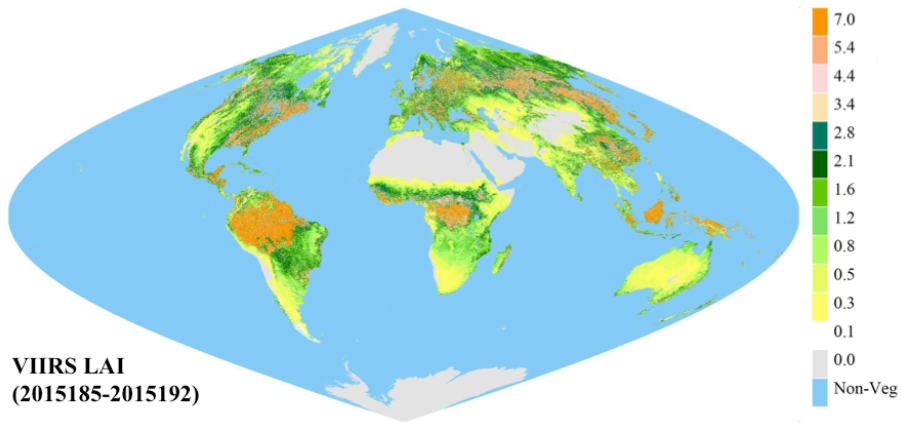
Table 3-1. LAI/FPAR products produced by Land SIPS

Product	ESDT	Description
LAI/FPAR (L4 Daily Tiled Products)	VNP15A1 [#]	<ul style="list-style-type: none"> • VIIRS/NPP LAI/FPAR Daily L4 500m Grid Product • Bands: I1 and I2 • Inputs: VNP09GA/VNP15IP and MCDLCHKM • Format: hdf5
LAI/FPAR (L4 8-day Composite Tiled Products)	VNP15A2 [*]	<ul style="list-style-type: none"> • VIIRS/NPP LAI/FPAR 8-day Composite Global SIN Grid Product • Bands: I1 and I2 • Inputs: VNP15A1 • Format: hdf5

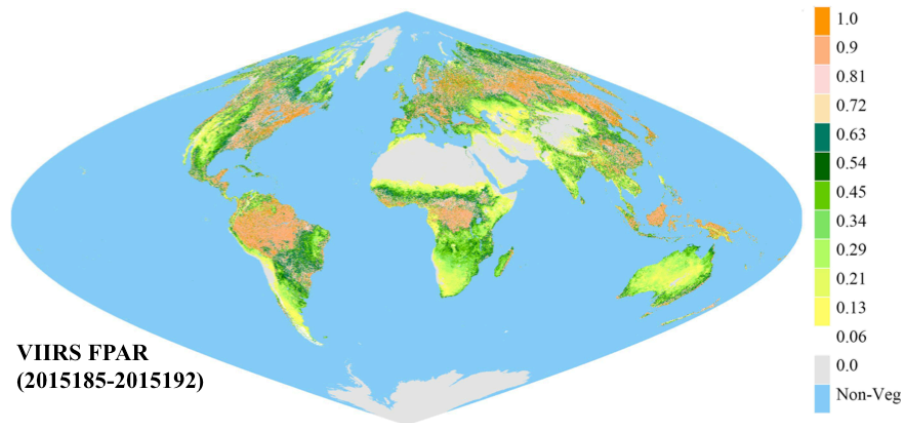
ESDT: Earth Science Data Type

[#]: Will be archived but not available to public.

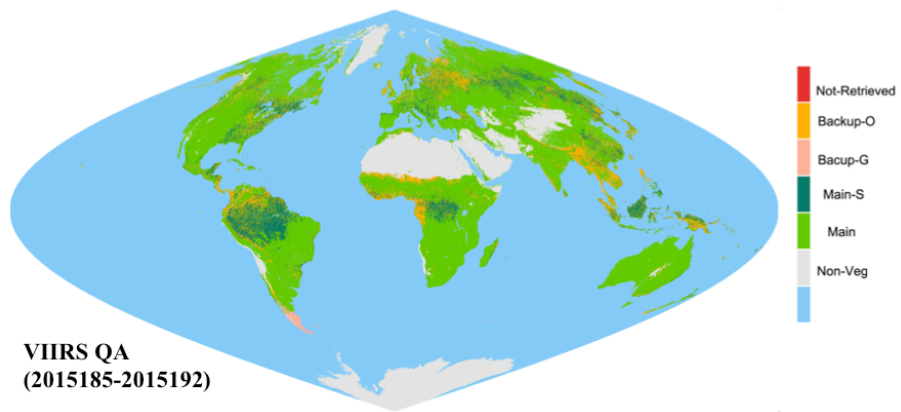
^{*}: Soon be available via Land Process Distributed Active Archive Center (<https://lpdaac.usgs.gov>)



(A)



(B)



(C)

Figure 3-1. Global color-coded maps of S-NPP VIIRS Version 1.0 LAI (A), FPAR (B) and algorithm path (C). These maps are generated from compositing process using 8-daily global LAI/FPAR retrievals based on optimally parameterized Look-Up Table (between 4 and 11 July 2015). Both quantities are dimensionless. Description for the legend of SCF_QC is given here: Main – Main algorithm was executed; Main-S - Main algorithm was executed. Saturation; BackUp-G - View/sun zenith angle too low. Backup retrievals; BackUp-O - Main algorithm fails. Backup retrievals; Not Retrieved - not executed because BRDF is not available.

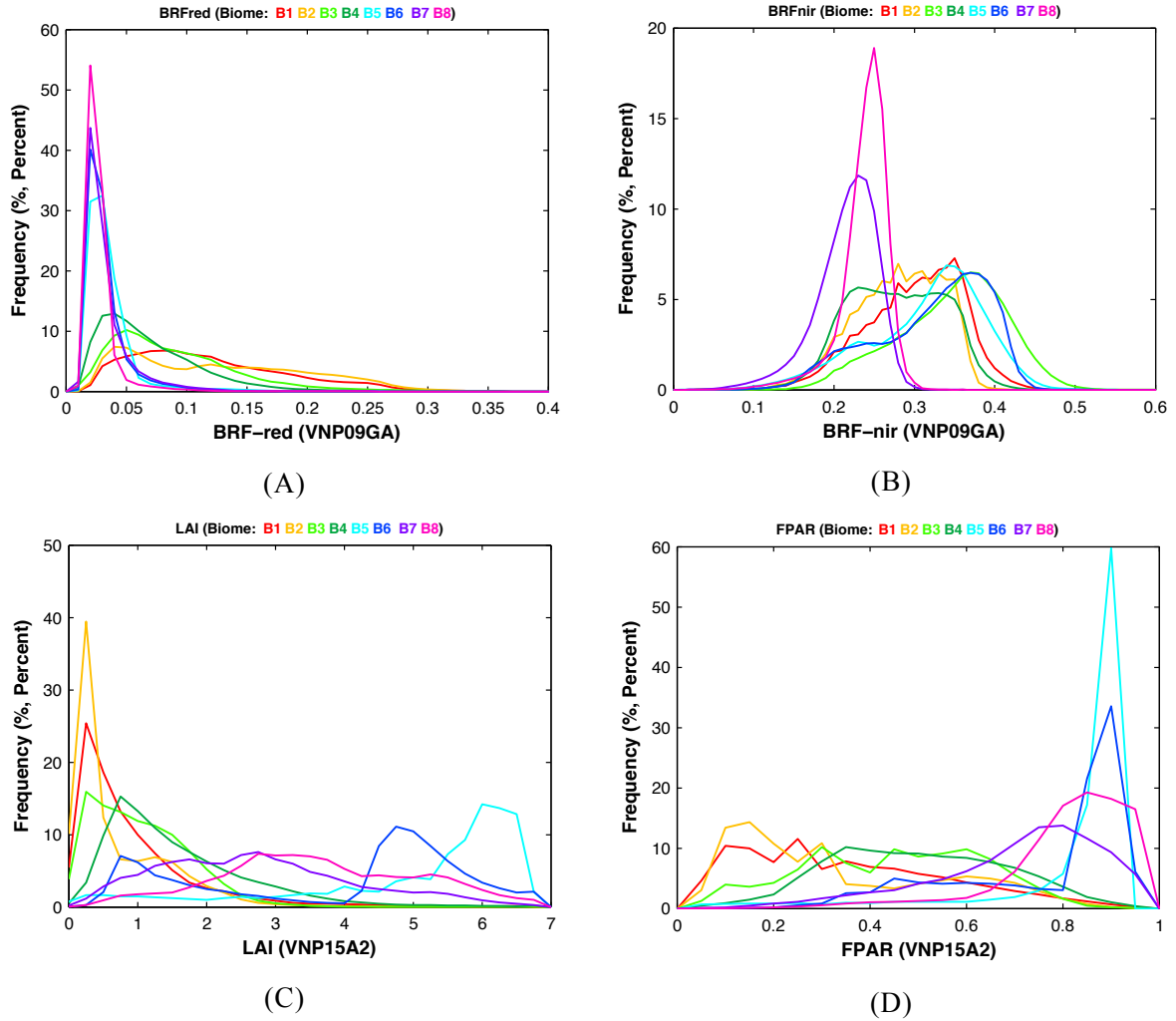


Figure 3-2. Histogram of canopy reflectances for global VIIRS VNP09GA data in July 2015 (DOY185-192) at red band (A), NIR (B) band. Histogram of retrieved LAI (C) and FPAR (D) based on optimally adjusted LUT. Colored lines represent each biome type, i.e., B1: Grasses/Cereal crops, B2: Shrubs, B3: Broadleaf crops, B4: Savanna, B5: Evergreen Broadleaf forest, B6: Deciduous Broadleaf forest, B7: Evergreen Needleleaf forest, B8: Deciduous Needleleaf forest.

3.2. Product Input

3.2.1 Spectral Bands

VNP09GA L2G 500m Surface Reflectance – I1 (red) and I2 (NIR) Band

The VIIRS Level 2G surface reflectance products called VNP09GA are composed of all available surface reflectance observations for a given day over a set of tiles with global coverage. The first set of observations for each data set and grid cell are stored as a two-dimensional data set. Additional data layers are stored in a compacted format. By calculating observation score based on QA and geometry information, the algorithm produces the intermediate surface reflectance product that contains the best quality observation (i.e., VNP15IP). Then it ingests the best quality observations only to produce LAI/FPAR retrievals. Theoretically, the LAI/FPAR algorithm can make use of multiple atmosphere-corrected BRFs and their uncertainties (Wang et al., 2001). In practice, due to increasing uncertainty level by incorporating more spectral bands (Knyazikhin et al., 1999), the algorithm only uses red and NIR (i.e., I1 and I2) bands for the operational production (See Figure 3-3). Details of VNP09GA can be found in Franch et al. (2016) and Roger et al. (2016).

3.2.2 Masks, Thresholds and Ancillary Data

The algorithm chooses a strategy to run through all available vegetated pixels without masking or screening process (e.g., cloud, aerosol and cloud shadow mask etc.) rather than pre-masking inputs before algorithm implementation. This is beneficial to minimize the impact of upstream products. The only required ancillary data for the LAI/FPAR algorithm is the global 8-biome map. Introducing this biome map enables simplified assumptions and standardized constants (e.g., vegetation and soil optical properties) that vary with biome and soil types only. Thus, using the biome map as prior-knowledge can reduce the number of unknowns of the “ill-posed” inverse problem (Myneni et al., 2002).

Global Land Cover Classification Map (Biome Map)

An accurate land cover map is a pre-requisite for choosing the appropriate relation between surface parameters (LAI and FPAR) and the satellite derived reflectances. The EOS MODIS LC science team has successfully provided global land cover maps at a 500m resolution with well-matured classification algorithm (C6). Several aspects of the algorithm have been improved: (a) Hierarchical classification

approach, (b) Random Forest classifier, (c) Improved training data, (d) Improved feature set and (e) Hidden Markov model (Gray et al., 2016). The map classifies global vegetation into eight biomes with different canopy and soil patterns (see Figure 2-3 and Table 2-1). The eight biomes are: (B1) grasses and cereal crops; (B2) shrubs; (B3) broadleaf crops; (B4) savannas; (B5) evergreen broadleaf forests; (B6) deciduous broadleaf forests; (B7) evergreen needleleaf forests and (B8) deciduous needleleaf forests. Areal proportion of each biome is given in Table 3-2. Note that input global biome map for developing VIIRS LAI/FPAR algorithm and its production is supported from MODIS LC product at this stage and will be updated with VIIRS data at a later date.

Table 3-2. Global biome map composition. This biome map composition is calculated from MODIS global biome map 2010 data which is used for VIIRS LAI/FPAR retrievals.

Biome ID	Biome Type	Proportion (%)
1	Grasses and Cereal crops	21.8
2	Shrubs	14.8
3	Broadleaf crops	2.8
4	Savannas	17.0
5	Evergreen broadleaf forests	10.0
6	Deciduous broadleaf forests	3.7
7	Evergreen needle leaf forests	4.3
8	Deciduous needle leaf forests	1.4

3.3. Production Logic and Data Flow

This section aims to briefly describe the data production logic and data flow scheme implemented in Land SIPS.

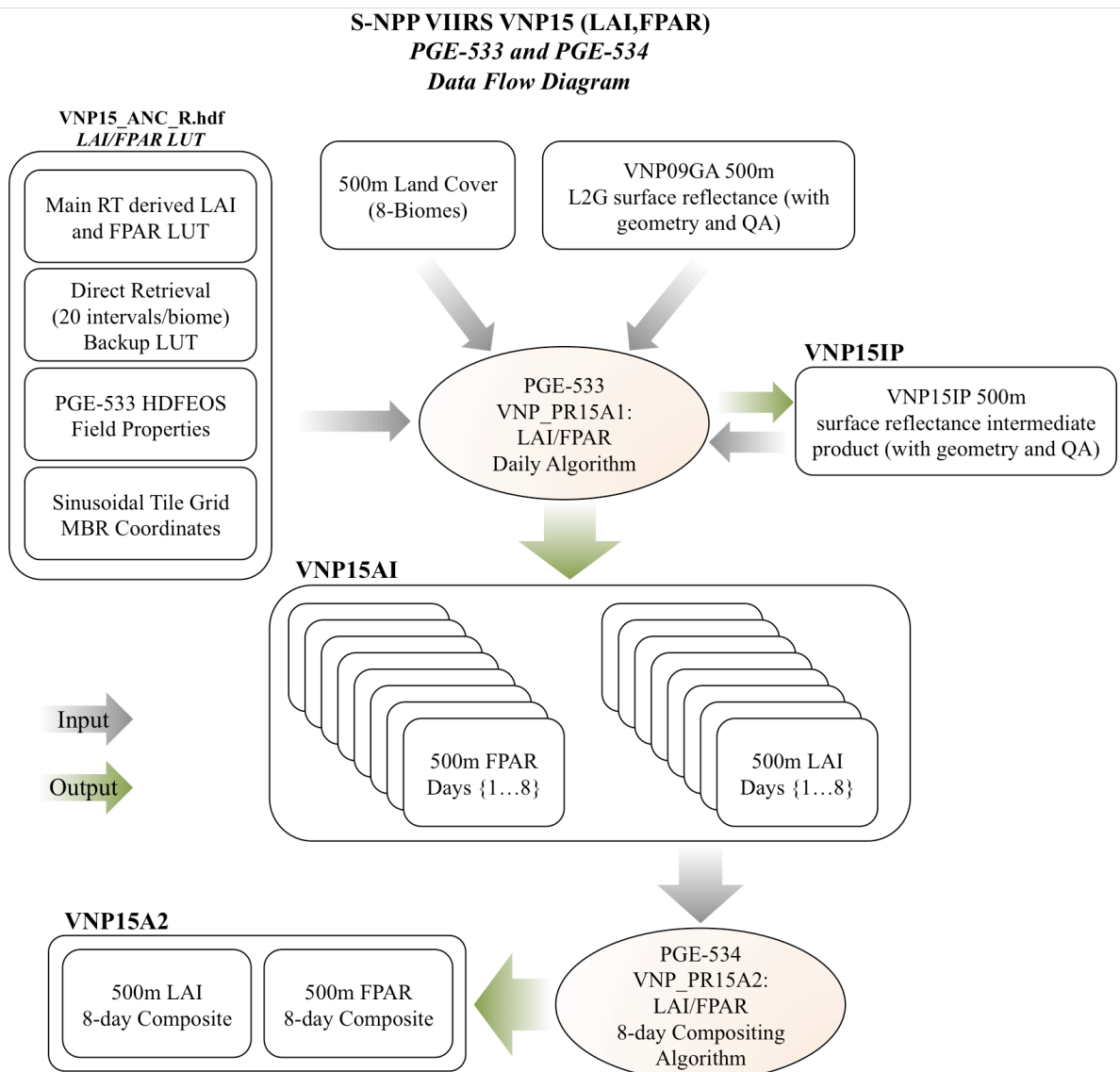


Figure 3-3. Algorithm flow of VIIRS LAI/FPAR Version 1 production. VIIRS LAI/FPAR operational production separates two algorithm steps: a) daily LAI/FPAR algorithm (refers to PGE533) and b) 8-day compositing algorithm (refers to PGE534). Spatially gridded 8 daily 500m L2G VNP09GA and biome map are introduced as inputs to generate 8 consecutive daily VNP15A1 products. Radiative Transfer (RT) theory based Main algorithm and empirical relation (LAI-NDVI or FPAR-NDVI) based back-up algorithm paths operate selectively. With 8-day compositing strategy, global 500m LAI/FPAR product (VNP15A2) is available. Note that daily LAI/FPAR algorithm ingests multiple observations from L2G surface reflectance and then generate the intermediate surface reflectance, geometry and QA (VNP15IP) for retrieval algorithm.

3.3.1. LAI & FPAR Algorithm - Daily Logic (PGE-533)

The following section briefly summarizes the high-level runtime logic implemented in VNP15A1:

- Upon initiation of the session (once per tile), the runtime inputs are retrieved from the process control file (.pcf) file provided by the high level scheduler/loader environment.
- The PGE allocates all in-memory data structures it requires, opens the static ancillary HDF-EOS file (VNP15A1_ANC_V1.hdf) and builds an in-memory dictionary of its contents.
- All spatial input HDF-EOS files are opened (land cover and 500 m surface reflectance files) and in-memory dictionaries are built of their contents.
- The daily candidate output file is created, using field properties read at runtime from the ancillary file.
- A row-wise processing loop is established, and each subsequent row from all input files is buffered into memory.
- A pixel-wise processing loop is established, and for each pixel, input fields are decoded from their digital representation (integer) to their biophysical form (floating point) using {gain, offset} calibration factors. QA fields from the inputs are also checked, in order to pass-through all pixels not classified as "land" or otherwise of unsuitable quality.
- The main RT based retrieval method is performed on the pixel, using the channel-wise reflectances and pixel geometry. An estimate of FPAR and LAI (and QA for each) is then calculated for the pixel.
- The biophysical estimates are encoded to their digital (integer) representations, and are placed in the output buffer.
- When the current row is complete, it is written out to the open HDF-EOS archive product file.
- When all rows are complete, final ECS metadata processing is performed, whereby the ECS metadata fields are set into their blocks, and finally written out to the product output file.
- Final session cleanup tasks are then performed, where all dynamic memory is released, files are closed.

3.3.2. LAI & FPAR Algorithm - 8-day Compositing Logic (PGE-534)

The VNP15A2 (PGE-534) executable accepts a set of candidate tiles produced by the daily VNP15A1 process, and composites these using a simple selection rule

whereby the pixel with the maximum FPAR (across the 8 days) is selected for inclusion in the output tile of identical format. Relevant QA and other tile-level metadata are taken from the day chosen to contribute its primary FPAR. The same day chosen to represent the FPAR measure also contributes the pixels LAI value. The VNP15A2 (PGE-534) executable is launched once every 8-day period, and is provided with the current 8-day set of VNP15A1 candidate daily tile products. It performs the following actions:

- Upon initiation of the session (once per tile), the runtime inputs are retrieved from the process control file (.pcf) provided by the high level scheduler/loader environment.
- The PGE allocates all in-memory data structures it requires; note this executable does not require the ancillary file, VNP15A2_ANC_V1.hdf.
- The set of candidate daily VNP15A1 product (from 1 to 8) files are opened, and in-memory dictionaries are built of their contents.
- A row-wise processing loop is established, and each subsequent row from each day's input file is buffered into memory.
- A pixel-wise processing loop is established, and for each pixel, the raw digital values are stored.
- An inner-most, temporal loop is established, looping through the (1 to 8) days of candidate data.
- From each set of 8 days pixels (e.g. using a vertical drill-down through the day dimension), the pixel with the highest FPAR value is identified. The base-0 index for this day is stored and used to retrieve the spatially coincident FPAR, LAI estimates associated with this day.
- The FPAR and LAI (and QC) values for the day identified above are then placed in the single 2D output buffer at the appropriate {line, sample} position.
- When the current row is complete, it is written out to the open HDF-EOS archive product file.
- When all rows are complete, final ECS metadata processing is performed, whereby the ECS metadata fields are set into their blocks, and finally written out to the product output file.
- Final session cleanup tasks are then performed, where all dynamic memory is released, files are closed.

4. Product Accuracy/Uncertainty

Accuracy is defined as the difference between the mean value of measurements and the corresponding true value. Uncertainty is defined as scatter (standard deviation) of measurements with respect to true value. The true values in these definitions refer to field measurements of LAI and FPAR. The accuracy and uncertainty of VIIRS LAI/FPAR products will be characterized via the following multiple approaches.

4.1. Validation Approach

Multiple validation techniques will be used to develop uncertainty information on SNPP VIIRS LAI/FPAR products. There has been an extensive effort since the inception of the NASA EOS program to validate biophysical products. Validation campaigns from existing network including the BigFoot, AERONET, FLUXNET, EOS Land Validation Core Sites and VALERI, with sustained efforts from several research teams across the globe that have provided the necessary platform to validate LAI/FPAR products (Morisette et al. 2006; Garrigues et al. 2008; Yan et al., 2016b). MODIS derived LAI/FPAR products, the predecessor of VIIRS, have been extensively validated over a suite of vegetation types and climatic regimes, and the product is categorized as a Stage 2 (Stage 1 for FPAR) land validated product under CEOS Land Product Validation (LPV) scheme. Thus VIIRS validation approach will adopt the EOS validation strategy that has been developed and refined over the past 17+ years. It is to be noted that “validation” of this strategy refers to both (a) direct and (b) indirect validation, where the former refers to comparing satellite derived measures with ground truth while the latter refers to an exercise intercomparing products from different sensor systems to test consistency. Both direct and indirect validation approaches provide a comprehensive knowledge about the accuracy of global LAI/FPAR products and level of uncertainties that may result due to input data and modeling errors.

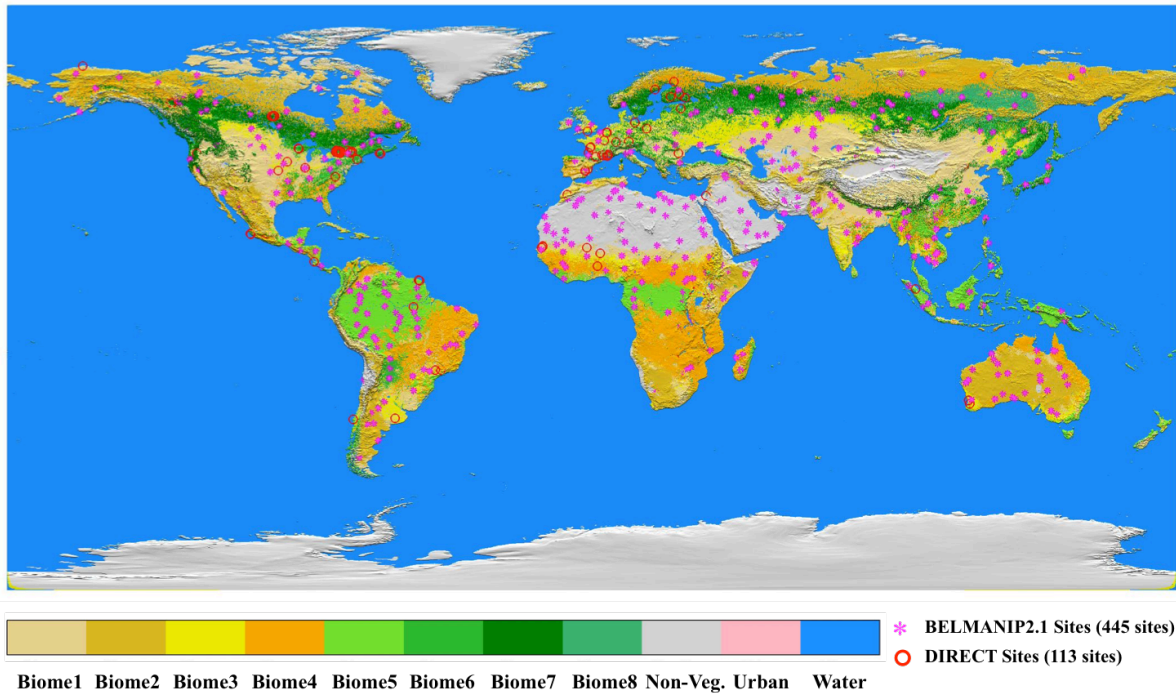


Figure 4-1. Global distribution of DIRECT & BELMANIP2.1 (BENchmark Land Multisite ANalysis and Intercomparison of Products) sites. The DIRECT is a collection of sites for which ground measurements are available and that have been collected (Garrigues et al., 2008) and processed according to the CEOS-LPV guidelines. The BELMANIP2.1 network of sites was designed to represent the global variability of vegetation types and climatological conditions (Barret et al., 2006). This network was mainly built using sites from existing experimental networks (FLUXNET, AERONET, VALERI, BigFoot, etc.) and complemented with additional sites from the GLC2000 land cover map. Global vegetation is stratified into eight canopy architectural types, or biomes. The eight biomes are (1) grasses and cereal crops, (2) shrubs, (3) broadleaf crops, (4) savannas, (5) evergreen broadleaf forests, (6) deciduous broadleaf forests, (7) evergreen needle leaf forests, (8) deciduous needle leaf forests.

4.1.1. Direct Validation

The “bottom-up” approach proposed by the CEOS LPV subgroup will be adopted in the direct validation practice (Fernandes et al., 2014; Yang et al., 2006). This strategy is designed to correlate the scale of *in situ* biophysical measurements (i.e., LAI and FPAR) to that of the remote sensing product using finer-resolution images to bridge their scale gaps (Tan et al., 2005). This method is based on a two-stage sampling strategy that uses multiple elementary sampling units (ESUs) to capture the variability across the extent of a site and repeats measurements within each ESU to capture the variability within the pixels of high-resolution imagery. Then, a transfer function is established between ground and radiometric data sets to produce reference maps. This scheme has been widely used to evaluate the uncertainties in current LAI/FPAR products (e.g., MODIS LAI/FPAR) and it is suitable for product validation over homogeneous or heterogeneous areas.

Based on “bottom-up” approach, all available *in situ* LAI/FPAR measurements over the globe will be synthesized for VIIRS LAI/FPAR assessment. In particular, the ImagineS project, which is designed to support European Copernicus Global Land Service, has conducted a series of single date or multi-temporal field campaigns over 23 sites around the world during the past 5-years (from 2013 to present) (<http://fp7-imagines.eu>). The measurements of LAI and FPAR have been up-scaled based on the above-mentioned scaling strategy and locally aggregated biophysical retrievals can be used for product assessment. This ImagineS project provides indispensable *in situ* data sets, as the field campaigns have been conducted in an unbiased acquisition mode. Furthermore, our long-running collaborations with European and Asian partners (Baret et al., 2006; Garrigues et al., 2008), who have active validation projects, enables to enlarge the available *in situ* data pool. One of these – VALERI - currently has over 40 active sites representing all the major vegetation classes from different continents. Field campaigns at several of these sites are likely during the next few years and those data will also be used to validate VIIRS LAI/FPAR products. Additional validation datasets are from a collection of sites (“DIRECT”) for which ground measurements have been collected during the early EOS era (mostly from 2000 to 2008) (Weiss et al., 2014). There are currently 113 such datasets available (Figure 4-1), corresponding to different sites and various dates of measurements. As the data sets were collected previously, temporal mismatch between ground measurements and VIIRS retrievals may induce unexpected bias or spurious assessment. Nevertheless, these ground measurements are valuable for obtaining multiple observations covering different spatiotemporal representativeness. Note that strict statistical test to justify the assumption (i.e., no significant change between acquisition year of ground and VIIRS) should be prioritized and results will be carefully interpreted.

To facilitate scaling efforts, an additional direct validation approach is planned. MALIBU (Multi AngLe Imaging Bidirectional Reflectance Distribution Function sUAS) is a new demonstration-instrument recently deployed on a prototype small Unmanned Aircraft System that is part of a series of pathfinder missions funded under NASA's Internal Research and Development (IRAD) Program (<https://viirsland.gsfc.nasa.gov/Campaigns.html>). Dual Tetracam cameras (with overlapping swaths) are mounted on the MALIBU platform across-track and their channels were specifically chosen to cover the relative spectral response of multiple

satellite land sensors including MISR, MODIS and SNPP/JPSS VIIRS. Multiple angular observations from MALIBU on various biome types will provide opportunities to explore the abilities of the RT model in LAI/FPAR algorithm and angular impact on retrieval or scaling.

4.1.3. Indirect Validation

VIIRS LAI/FPAR products will be compared with products from other moderate resolution sensors including MODIS, SPOT and AVHRR in order to identify their respective strengths and weaknesses, thus leading to improvements in the next generation (version) of products. These exercises also help to improve user confidence in the research-quality of VIIRS products. In particular, the consistency evaluation between VIIRS and MODIS retrievals is prioritized in our work in order to build a long time series that is independent of sensor data. The intercomparison will be performed at various scales – global, regional and local (validation sites). At the global and regional scales, typically, the products will be re-projected to a common projection, re-sampled to a coarse spatial (5-km) and temporal (monthly) resolution. Several temporal composites for each of the four seasons will be selected to assess temporal variations in the products. The following statistical characteristics of the data sets will be evaluated: histograms of LAI by vegetation type, differences between global maps and transects across a range of latitudes, and statistics on data quality. The site-level comparison will be performed with product time series at fine spatial and temporal resolutions. Sites from the BELMANIP2.1 (Benchmark Land Multisite Analysis and Intercomparison of Products) network (Baret et al., 2006), which includes existing experimental networks (FLUXNET, AERONET, VALERI, BigFoot, etc.), will be introduced (Figure 4-1). This network is beneficial for intercomparison framework as the site selection was performed for each band of latitude (10° width) by keeping the same proportion of biome types within the selected sites as within the whole latitude band. Thus the selected sites are homogeneous over a 10×10 km² area, nearly flat terrain and with a minimum proportion of urban area and permanent water bodies. Representing the latest version, the BELMANIP2.1 currently contains 445 sites and is used in this validation approach. We have previously performed similar inter-comparison exercises with EOS LAI/FPAR products (Yan et al., 2016b). The VIIRS products will be assessed in a similar manner.

4.2. Preliminary Assessment

4.2.1. Direct Validation

Figures 4-2A and 4-2B compare ground measured LAI and FPAR with those of VIIRS, respectively. As expected, VIIRS shows better agreement with true LAI than with effective LAI. VIIRS retrievals are found to systematically overestimate effective LAI measurements, especially at the high LAI range (Stenberg et al., 1996). Overall, most of the data are within ± 1 LAI bias, indicating that the total uncertainty of this validation work is less than 1 LAI unit (RMSE = 0.67). For FPAR, the R^2 and RMSE are 0.81 and 0.1, respectively. The results present a tendency for overestimation by VIIRS retrievals. This systematic overestimation of FPAR over sparsely vegetated areas has been reported as a main drawback of the current version of the algorithm (Camacho et al., 2013). However, the disagreement in this preliminary assessment may also be due to the fact that understories are usually not taken into account in ground measurements that underestimate the true FPAR (Majasalmi et al., 2015). Overall, most data are within ± 0.2 bias with all uncertainties included. Note that, this uncertainty comes from both VIIRS products and other sources including uncertainties of reference maps and mismatch in spatial and temporal domains. It should also be noted that the distribution of measurements is problematic with an over representation of low values and non-woody vegetation. Adding more ground measurements, especially from forest biomes, may resolve this issue according to guidelines from CEOS/WGCV-LPV.

4.2.2. Indirect Validation (Consistency Evaluation)

While it is critical that LAI/FPAR products are generated with high accuracy and precision, more importantly they must be produced with consistent algorithms across different sensor platforms in order to maintain a continuous and well characterized data record. This is especially important for the VIIRS LAI/FPAR product on SNPP, which bridges the gap between NASA's EOS satellites and the next generation JPSS platforms. Thus, to evaluate the spatiotemporal consistency between VIIRS and MODIS LAI/FPAR products, one-year time series of VIIRS and MODIS (Aqua) LAI/FPAR over selected regions have been retrieved and their consistency is evaluated at two different scale-levels: regional and site scales. Global scale evaluation and more explicit analysis will follow this preliminary evaluation once VIIRS era global products are available.

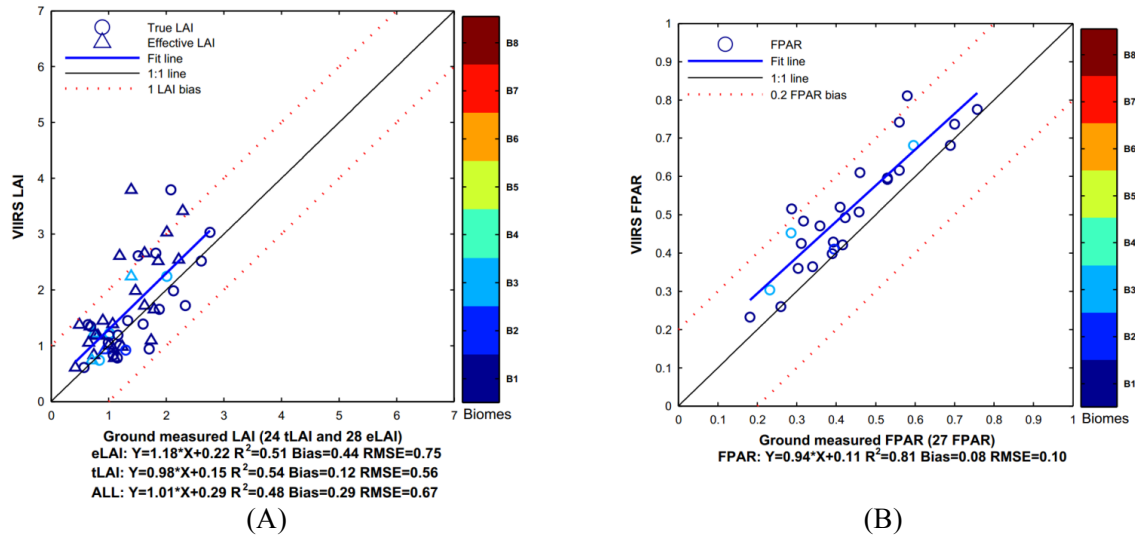


Figure 4-2. Comparisons between ground measurements and VIIRS retrievals. (A) LAI and (B) FPAR. 24 true LAI, 28 effective LAI and 27 FPAR measurements are available for comparison purpose. The 3km×3km sites dominated by different biome types are depicted by different colors. Circles (triangles) in panel (A) represents ground LAI measurements corrected (not corrected) for clumping. Note that these comparisons use only temporally matched observations (only ImagineS)

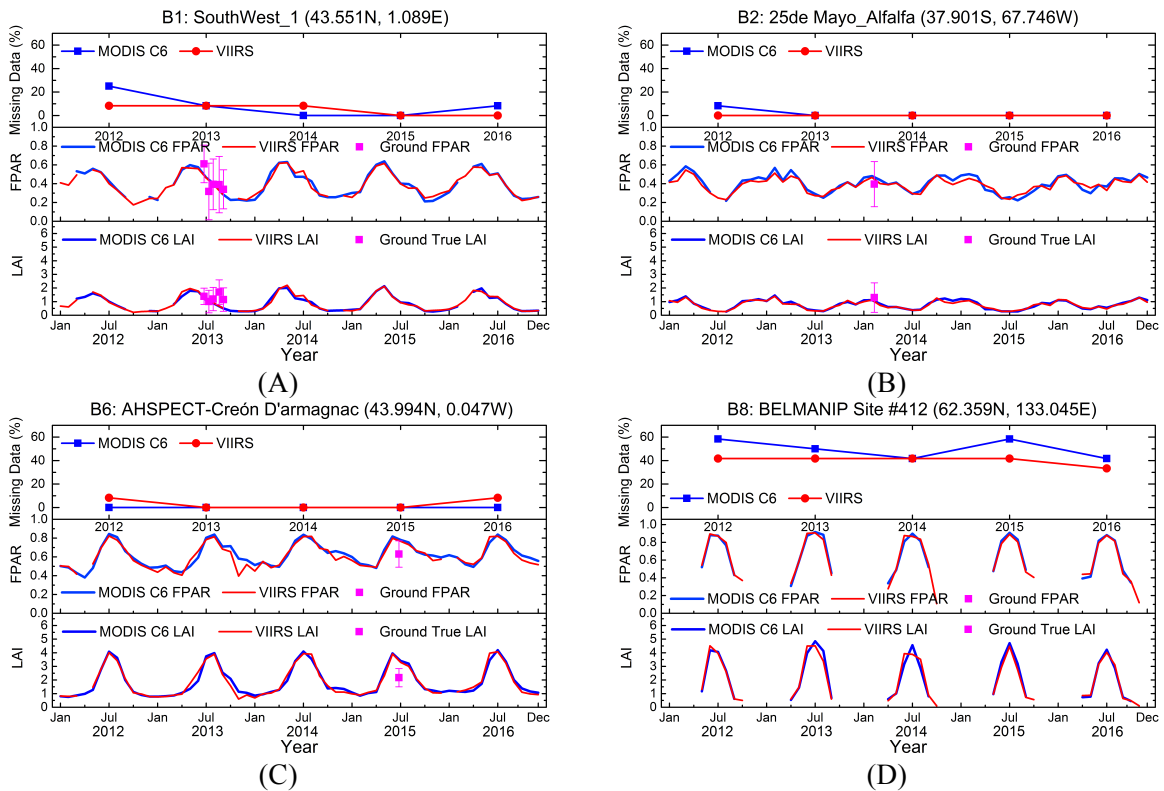


Figure 4-3. Temporal comparisons of LAI and FPAR of VIIRS V1 and Aqua MODIS C6 (MYD15A2H) products over four validation sites. Monthly averaged LAI and FPAR values for the time period from 2012 to 2016 are shown here. Blue and red lines stand for MODIS C6 and VIIRS respectively. Upper panel shows missing data rate in each year and following two panels show seasonal variation of LAI/FPAR products with collected ground measurements. Panel (A), (B), (C) and (D) are for grasses/cereal crops (Biome1), shrubs (Biome2), deciduous broadleaf forest (Biome6) and deciduous needleleaf forest (Biome8) cases, respectively. Note that the ground measurement plotted in panel (C) is not valid when the entropy criterion is applied. This means that higher heterogeneity may result in about 1 LAI unit difference.

Site-Scale

Multiple validation sites and BELMANIP2 network are used to evaluate site-scale VIIRS-MODIS consistency. Figure 4-3 shows the seasonal trajectory of VIIRS and MODIS LAI/FPAR products over four sites for the period from 2012–2016. All available ground measurements are plotted in these figures as a reference. Statistics of these temporal comparisons are given in Table 4-1. Note that the result reported in Table 4-1 is limited by only 2015 data. Both products shown in Figure 4-3 achieve a good temporal continuity across all biomes and comparable spatial coverage (i.e., missing data rate). Each site shows distinct characteristics of seasonal variations. For example, non-forest biomes exhibit smaller seasonal amplitude changes, less than 2 LAI (0.4 FPAR), while forest biomes reveal a stronger LAI (4 LAI) and FPAR (0.5 FPAR) seasonality during the annual cycle. Interestingly, the algorithms implemented for both sensors capture the ground measurements well and also enable differentiation of possible negative impacts due to snow or cloud contamination. Over the 445 BELMANIP2.1 sites, the statistical result from temporal evaluation at site-scale indicates good consistency between VIIRS and MODIS in both LAI/FPAR retrievals. Most biomes, except biomes 5 and 7, exhibit high values of R^2 (greater than 0.9) but the dense evergreen broadleaf forests (B5) show less agreement in both LAI/FPAR. This is not surprising because of sub-optimal quality of retrievals due to reflectance saturation.

Table 4-1. Site-scale comparison between VIIRS and MODIS LAI/FPAR retrievals for the period of 2012–2016. Multiple validation sites and BELMANIP2 network are introduced for this comparison. Linear least square regression

Biome	LAI					FPAR				
	a	b	R^2	Bias	RMSE	a	b	R^2	Bias	RMSE
1	0.927	0.046	0.96	-0.009	0.16	0.953	0.015	0.98	0.000	0.03
2	0.942	0.029	0.97	0.006	0.07	0.966	0.011	0.97	0.003	0.02
3	0.845	0.130	0.96	-0.045	0.25	0.918	0.034	0.97	-0.002	0.04
4	0.909	0.139	0.91	0.015	0.27	0.923	0.036	0.94	0.001	0.04
5	0.779	1.206	0.59	-0.076	0.63	0.707	0.254	0.47	-0.004	0.04
6	0.965	0.098	0.93	0.008	0.53	0.913	0.059	0.92	0.004	0.07
7	0.910	0.194	0.73	0.010	0.56	0.862	0.088	0.75	-0.004	0.07
8	0.968	0.064	0.94	-0.011	0.40	0.963	0.022	0.95	-0.002	0.05

Biome1: Grasses/Cereal crops, Biome2: Shrubs, Biome3: Broadleaf crops, Biome4: Savanna, Biome5: Evergreen Broadleaf forest, Biome6: Deciduous Broadleaf forest, Biome7: Evergreen Needleleaf forest, Biome8: Deciduous Needleleaf forest.

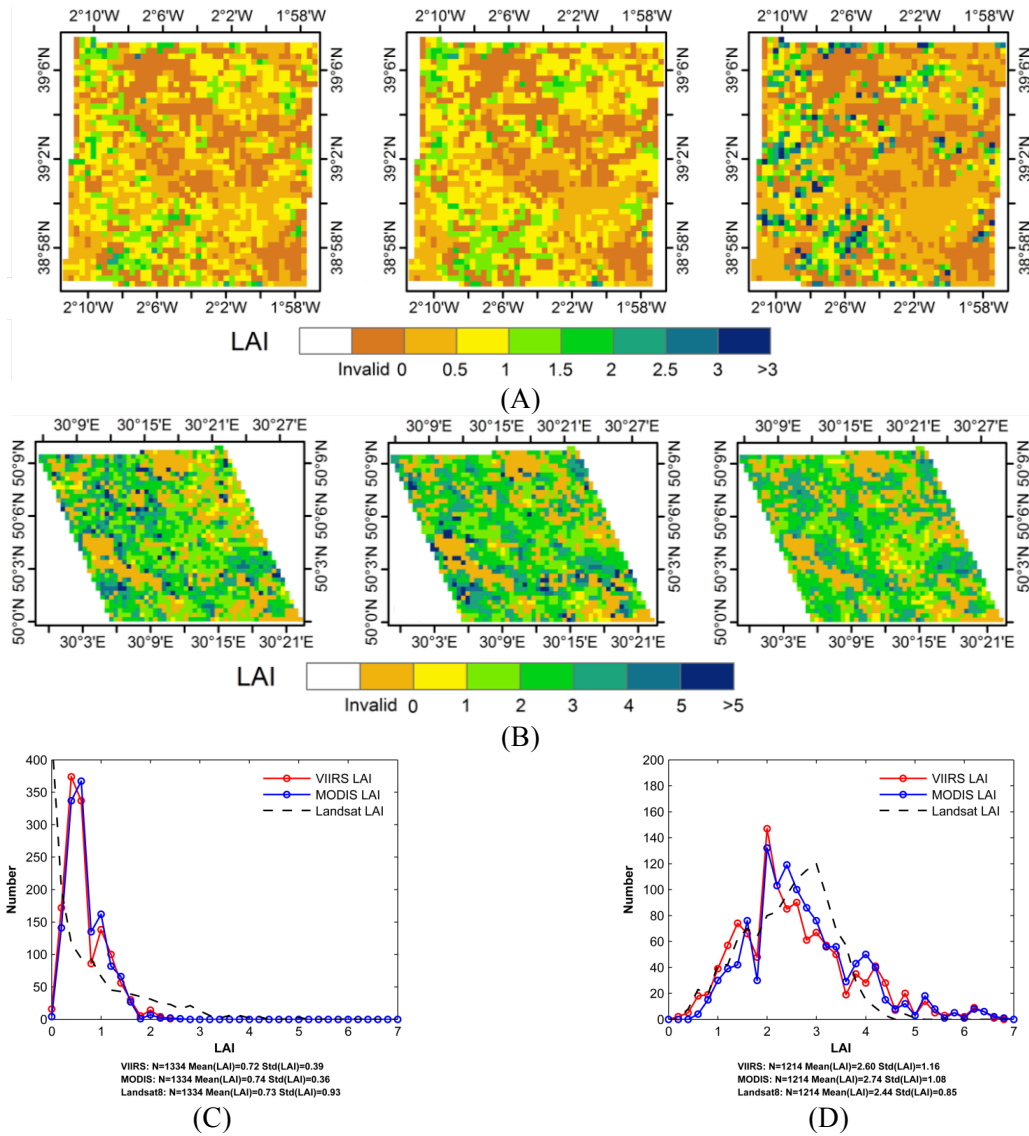


Figure 4-4. Spatial distribution of retrieved VIIRS, MODIS and Landsat LAIs at over Barrax (A) in Spain and Pshenichne site (B) in Ukraine. The Landsat LAI retrievals for Barrax and Pshenichne are acquired in 05/27/2015 and 06/12/2014, and then firstly derived raw spatial resolution (30m) then aggregated to 500m-resolution for comparison purpose. Well-characterized transfer functions between ground truth and Landsat spectral information are used to build Landsat LAI reference maps. Corresponding histograms for LAIs for two sites are given in (C) and (D), respectively.

Figure 4-4 presents the spatial distribution of VIIRS, MODIS and Landsat LAI retrievals at 500m resolution over two select validation sites (Barrax in Spain and Pshenichne in Ukraine). Dominant biomes are cropland and deciduous broadleaf forest, respectively. Overall, VIIRS closely resembles the spatial distribution and histogram of MODIS LAI over both sites. The degree of similarity between moderate- (i.e., VIIRS and MODIS) and finer- resolution retrievals is lower in the heterogeneous cropland site and higher in the more homogeneous dense forest. This discrepancy is likely explained by intensified scale effect with increasing heterogeneity. Tian et al.

(2002) demonstrated that LAI retrieval errors at coarse resolution are inversely related to the proportion of the dominant land cover in such pixels. Similar patterns are also observed in the case of FPAR (not shown here).

Regional-Scale

Two separate investigations are performed in the regional scale evaluation of consistency: (a) continental- and (b) tile- scale. An 8-day LAI composite (between 4 and 11 July 2015) over the African continent and 1-year long retrievals over selected tiles (8 tiles for 8 biomes) are used. The spatial distributions of LAI from both sensors over the African continent during an 8-day composite period are compared in [Figure 4-5A](#). There is no visually distinguishable difference between the two datasets. VIIRS and MODIS LAI exhibit similar and continuous spatial patterns over the whole continent. As expected, the LAI patterns closely coincide with the spatial distribution of the vegetation type—high LAI over forests and low LAI over herbaceous vegetation. The tropical evergreen forests in the Congo basin have high LAI values (up to 7); regions somewhat covered by grasses and shrubs generally have low LAIs. From the absolute LAI difference map ([Figure 4-5C](#)), VIIRS is found to spatially agree with MODIS well, with absolute differences within ± 0.5 LAI unit for most of the land surface ([Figure 4-5D](#)). However, obvious differences over densely vegetated regions (Congo rainforests) can be observed. These discrepancies between VIIRS and MODIS can exceed 1 LAI unit. The differences are stochastic and do not reflect a systematic bias. This is clearly explained by a mismatch in algorithm path for LAI retrieval ([Figure 4-5B](#)). The RT-based main algorithm without saturation condition delivers the best quality of retrieval. And sub-optimal and less accurate retrievals are generated via the main algorithm under reflectance saturation and the empirical back-up algorithm, respectively. Thus, careful interpretation of the retrievals over densely vegetated regions by consulting the QA is recommended.

The scatter plots in [Figure 4-6](#) show the comparison between VIIRS and MODIS LAI/FPAR over the entire year of 2015. The color-coded 46 circles in each plot represent the averaged LAI/FPAR values of biome-specific pixels during the corresponding 8-day composites. As expected by the RT theory, LAI and FPAR show good consistency in temporal variation. Note that the LAI/FPAR differences between two neighboring 8-day composites vary, which means that the rate of LAI or FPAR

change varies. VIIRS LAI and FPAR agree with MODIS products very well, with R^2 values larger than 0.99 across biomes without any obvious systematic bias.

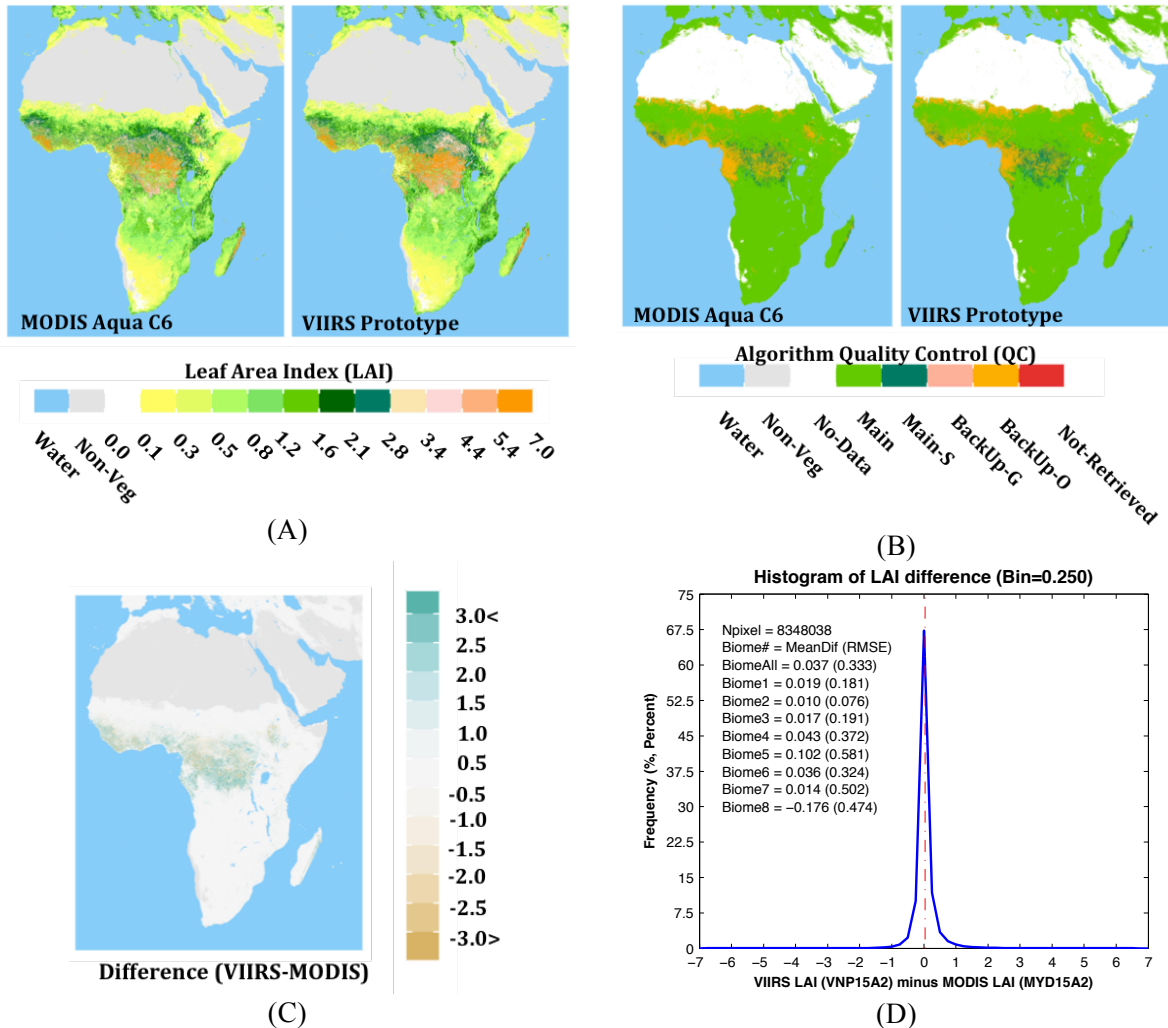
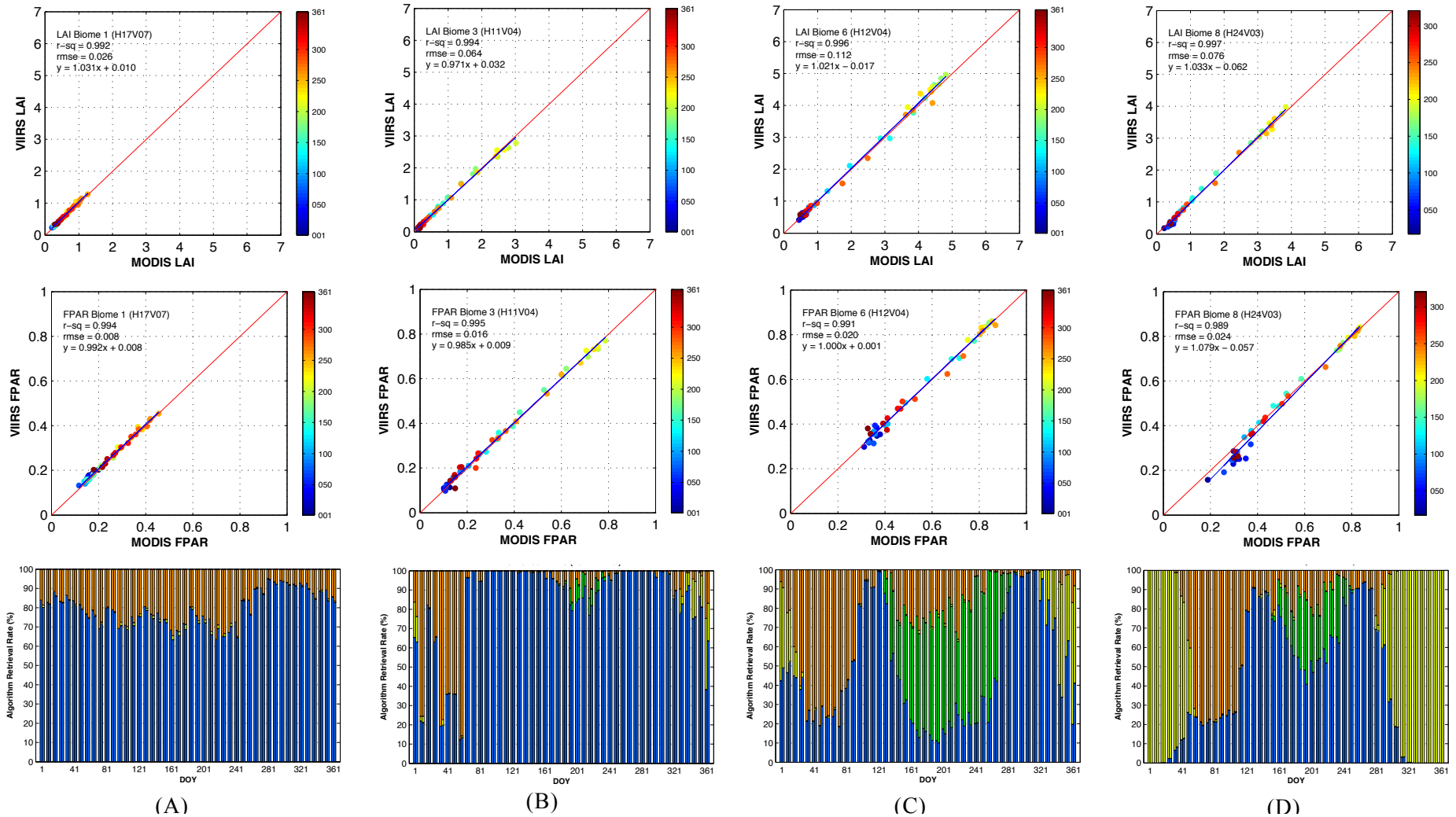


Figure 4-5. (A) Retrieved and VIIRS V1 and Aqua MODIS LAI over Africa region with their own LUT configuration. Overall spatial distribution of VIIRS LAI is closely resembled with MODIS LAI. (B) Algorithm retrieval rate (%) of VIIRS and Aqua MODIS. Legends: Main – Main algorithm was executed; Main-S - Main algorithm was executed. Saturation; Backup-G -View/sun zenith angle too low. Backup retrievals; Backup-O - Main algorithm fails. Backup retrievals; Not Retrieved - not executed because BRF is not available. (C) Spatial distribution of LAI difference between VIIRS and MODIS. (D) Histogram of the difference.

The algorithm path is also critical to the consistency between two products as it impacts LAI/FPAR accuracy. It varies by vegetation density, sun-sensor geometry and atmospheric conditions. Thus, algorithm path will exhibit seasonality as well. Panels in [third row of Figure 4-6](#) show the annual variation of algorithm retrieval rate through the year 2015 over four select tiles. A clear seasonality can be seen and the RI (i.e., the rate of main algorithm retrieval with- and without-saturation condition) in winter season is much lower than that in other seasons. This is due to poor geometry and ice/snow

coverage in winter. Non-forest biomes (i.e., Biome 1 and 3) situated in medium to low latitudes have very high main algorithm retrieval rate (>90%) during the growing season. This ensures a higher accuracy of LAI/FPAR retrievals and is meaningful for the use of these products in crop yield estimation (Doraiswamy et al., 2004). We note a large proportion of main algorithm saturation from May to October over deciduous forests (third row of Figure 4-6C), which reduces the accuracy of the products. Higher backup algorithm rates in winter are found in biomes located in high latitudes where larger solar zenith angle limits main algorithm retrieval. The results in general depict good consistency in algorithm path between VIIRS and MODIS year round and in all biomes. This imbues confidence in the VIIRS-MODIS LAI/FPAR products.



5. Data Formats

5.1. Formats

SNPP VIIRS LAI/FPAR data are provided in the standard land HDF5-EOS (Hierarchical Data Format 5 - Earth Observing System) format, which is beneficial to efficiently manage multidimensional arrays of NASA science records and structures for grouping objects. VIIRS product filenames (i.e., the local granule ID) follow a naming convention that gives useful information regarding the product. For example, the filename VNP15A2.A2015345.h28v05.001.2016292234657.h5 indicates:

- VNP15A2 – Product Short Name
- .A2015345 – Julian Date of Acquisition (A–YYYYDDD)
- .h28v05 – Tile Identifier (horizontal XX, vertical YY)
- .001 – Product Version
- .2016292234657 – Julian Date of Production (YYYYDDDDHHMMSS)
- .h5 – Data Format (HDF5–EOS)

The product is composed of six different Scientific Data Set (SDS) layers. Details are given in [Table 5-1](#).

Table 5-1. Scientific Data Sets included in the VIIRS LAI/FPAR product

Scientific Data Sets (HDF Layers) (6)	Units	Bit Type	Fill Value	Valid Range	Multiply By Scale Factor
Fpar	Dimensionless (Fraction)	8-bit unsigned integer	249–255	0–100	0.01
Lai	Dimensionless (m ² plant/m ² ground)	8-bit unsigned integer	249–255	0–100	0.1
FparLai_QC	Class flag	8-bit unsigned integer	255	0–254	N/A
FparExtra_QC	Class flag	8-bit unsigned integer	255	0–254	N/A
FparStdDev	Dimensionless (Fraction)	8-bit unsigned integer	248–255	0–100	0.01
LaiStdDev	Dimensionless (m ² plant/m ² ground)	8-bit unsigned integer	248–255	0–100	0.1

5.2. QC Metadata

Pixel-wise QC information of tiled VIIRS LAI/FPAR product is represented by

two SDS layers (FparLai_QC and FparExtra_QC) (See [Table 5-1](#)). Note that the LAI/FPAR algorithm is executed irrespective of input quality. Therefore user should consult the QC layers of the LAI/FPAR product to select reliable retrievals. The key indicator of retrieval quality of the LAI/FPAR product is SCF_QC bit field in FparLAI_QC SDS layer that represents algorithm path. Details of quality flags of the product are shown in following tables ([Table 5-2 and 5-3](#))

Table 5-2. Values of FparLAI_QC (8-bit)

Bit No.	Parameter Name	Bit Comb.	FparLAI_QC
0-2	SCF_QC (five-level confidence score)	000	0 Main (RT) method used, best result possible (no saturation)
		001	1 Main (RT) method used with saturation. Good, very usable
		010	2 Main (RT) method failed due to bad geometry, empirical algorithm used
		011	3 Main (RT) method failed due to problems other than geometry, empirical algorithm used
		100	4 Pixel not produced at all, value couldn't be retrieved (possible reasons: bad L1B data, unusable VNP09GA data, water pixel)
3	DeadDetector	0	Both red and NIR detectors are fine
		1	At least one band has dead detector
4-7	BiomeType	0000	0 Water
		0001	1 Grasses/cereal crops
		0010	2 Shrubs
		0011	3 Broadleaf crops
		0100	4 Savanna
		0101	5 Evergreen broadleaf forest
		0110	6 Deciduous broadleaf forest
		0111	7 Evergreen needleleaf forest
		1000	8 Deciduous needleleaf forest
		1001	9 Non-vegetated
		1010	10 Urban
		1011	11 Unclassified
1100	12 Filled Value		

Table 5-3. Values of FparExtra_QC

Bit No.	Parameter Name	Bit Comb.	FparExtra_QC
0-1	Cloud detection and confidence	00	0 Confident clear
		01	1 Probably clear
		10	2 Probably cloudy
		11	3 Confident cloudy
2	Cloud shadow	0	0 No cloud shadow
		1	1 Shadow
3	Thin cirrus	0	0 No
		1	1 Yes
4-5	Aerosol quantity	00	0 Climatology
		01	1 Low
		10	2 Average
		11	3 High
6	Snow/Ice	0	0 No
		1	1 Yes

And fill value legends for SDS layers are given in [Table 5-4](#) and [5-5](#).

Table 5-4. LAI and FPAR Fill value Legends

Value	Description
255	Fillvalue, assigned when: the VNP09GA surface reflectance for channel VIS, NIR was assigned as Fillvalue, or land cover pixel itself was assigned Fillvalue 255 or 254
254	land cover assigned as perennial salt or inland fresh water
253	land cover assigned as barren, sparse vegetation (rock, tundra, desert)
252	land cover assigned as perennial snow, ice
251	land cover assigned as “permanent” wetlands/inundated marshlands
250	land cover assigned as urban/built-up
249	land cover assigned as “unclassified” or not able to determine

Table 5-5. STD LAI and STD FPAR Fill Value Legends

Value	Description
255	Fillvalue, assigned when: the VNP09GA surface reflectance for channel VIS, NIR was assigned its Fillvalue, or land cover pixel itself was assigned Fillvalue 255 or 254
254	land cover assigned as perennial salt or inland fresh water
253	land cover assigned as barren, sparse vegetation (rock, tundra, desert)
252	land cover assigned as perennial snow, ice
251	land cover assigned as “permanent” wetlands/inundated marshlands
250	land cover assigned as urban/built-up
249	land cover assigned as “unclassified” or not able to determine
248	No standard deviation available, pixel produced using backup method

5.3. Spatial Projection

The VNP15 algorithms, like most VIIRS Land processes, are organized to accept global coverage inputs, and produce global coverage either daily (PGE-533) or on an 8-day (PGE-534) time step. Rather than process synoptic 500 m spatial resolution images, the VIIRS Land team has adopted a contiguous land tile scheme, based on the

Sinusoidal Grid - a map projection derived from the sinusoidal map projection. This projection defines a total of 648 tiles globally, at 10 degree resolution (https://modis-land.gsfc.nasa.gov/MODLAND_grid.html). The figure below graphically depicts the sinusoidal tile grid (assuming standard 10 degrees processing tiles) that we expect to work with at-launch (Figure 5-1). Each individual tile in this grid includes approximately 2400 x 2400 500 m pixels:

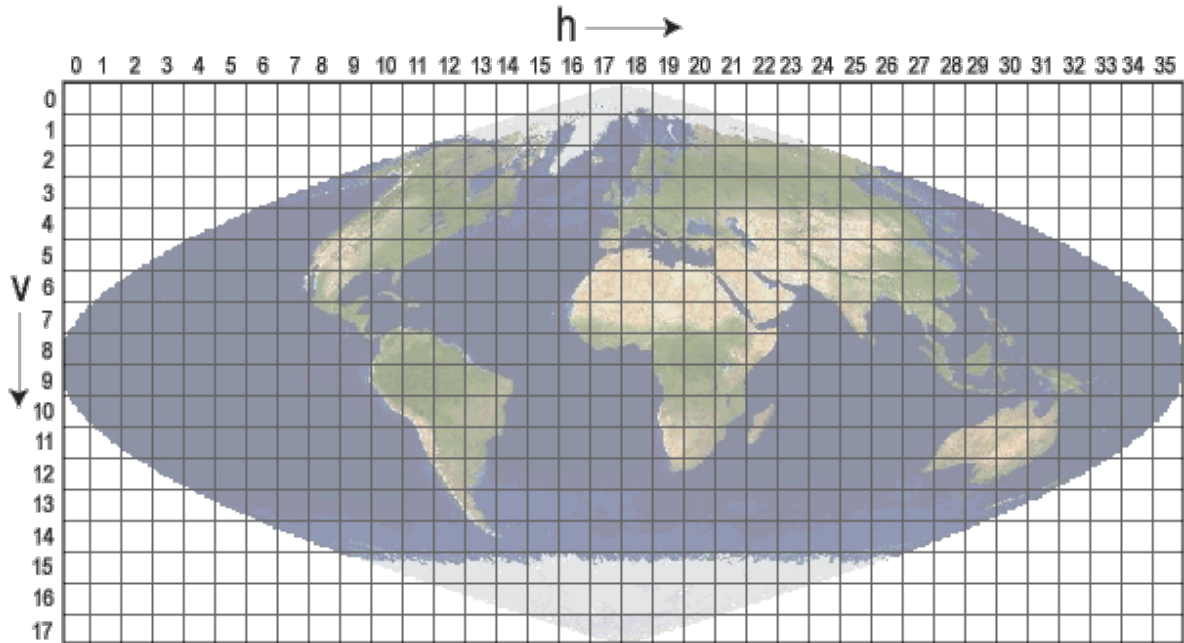


Figure 5-1. The Suomi-NPP VIIRS sinusoidal grid consists of 460 non-overlapping tiles which measure approximately $10^{\circ} \times 10^{\circ}$ region. This sinusoidal grid projection and tiling scheme are exactly consistent with MODIS land products.

6. Product Publications

- Yan, K., Park, T., Chen, C., Xu, B., Song, W., Yang, B., Zeng, Y., Liu, Z., Yan, G., Knyazikhin, Y. and Myneni, R.B., 2018. Generating Global Products of LAI and FPAR From SNPP-VIIRS Data: Theoretical Background and Implementation. *IEEE Transactions on Geoscience and Remote Sensing*.
- Xu, B., Park, T., Yan, K., Chen, C., Zeng, Y., Song, W., Yin, G., Li, J., Liu, Q., Knyazikhin, Y. and Myneni, R.B., 2018. Analysis of Global LAI/FPAR Products from VIIRS and MODIS Sensors for Spatio-Temporal Consistency and Uncertainty from 2012–2016. *Forests*, 9(2), p.73.

7. References

- Asrar, G.Q., Fuchs, M., Kanemasu, E.T. and Hatfield, J.L., 1984. Estimating absorbed photosynthetic radiation and leaf area index from spectral reflectance in wheat. *Agronomy journal*, 76(2), pp.300-306.
- Baret, F., Jacquemoud, S. and Hanocq, J.F., 1993. The soil line concept in remote sensing. *Remote Sensing Reviews*, 7(1), pp.65-82.
- Baret, F., Weiss, M., Lacaze, R., Camacho, F., Makhmara, H., Pacholczyk, P. and Smets, B., 2013. GEOV1: LAI and FAPAR essential climate variables and FCOVER global time series capitalizing over existing products. Part1: Principles of development and production. *Remote Sensing of Environment*, 137, pp.299-309.
- Bontempi, P. 2015. 'ROSES Selections and the MODIS and VIIRS Science Teams'. 2015 MODIS/VIIRS Science Team Meeting, 19-22 May 2015, Silver Spring, Maryland, USA.
- Bronshtein, I.N. and Semendyayev, K.A.F., 2013. *Handbook of mathematics*. Springer Science & Business Media.
- Camacho, F., Cernicharo, J., Lacaze, R., Baret, F. and Weiss, M., 2013. GEOV1: LAI, FAPAR essential climate variables and FCOVER global time series capitalizing over existing products. Part 2: Validation and intercomparison with reference products. *Remote Sensing of Environment*, 137, pp.310-329.
- Chen, J.M. and Black, T.A., 1992. Defining leaf area index for non-flat leaves. *Plant, Cell & Environment*, 15(4), pp.421-429.
- Doraiswamy, P.C., Hatfield, J.L., Jackson, T.J., Akhmedov, B., Prueger, J. and Stern, A., 2004. Crop condition and yield simulations using Landsat and MODIS. *Remote Sensing of Environment*, 92(4), pp.548-559.
- Franch, B., Roger, J.C. and Vermote, E.F. 2016. Suomi-NPP VIIRS Surface Reflectance Algorithm Theoretical Basis Document (ATBD) – Version 2.0. viewed 1 March 2017, from https://viirsland.gsfc.nasa.gov/PDF/ATBD_VIIRS_SR_v2.pdf
- Fernandes, R., Plummer, S. and Nightingale, J., 2014. Global Leaf Area Index Product Validation Good Practices. CEOS Working Group on Calibration and Validation-Land Product Validation Sub-Group. Version 2.0. viewed 1 January 2016, from https://lpvs.gsfc.nasa.gov/PDF/CEOS_LAI_PROTOCOL_Aug2014_v2.0.1.pdf
- Ganguly, S., Samanta, A., Schull, M.A., Shabanov, N.V., Milesi, C., Nemani, R.R., Knyazikhin, Y. and Myneni, R.B., 2008. Generating vegetation leaf area index Earth system data record from multiple sensors. Part 2: Implementation, analysis and validation. *Remote Sensing of Environment*, 112(12), pp.4318-4332.
- Ganguly, S., Schull, M.A., Samanta, A., Shabanov, N.V., Milesi, C., Nemani, R.R., Knyazikhin, Y. and Myneni, R.B., 2008. Generating vegetation leaf area index earth system data record from multiple sensors. Part 1: Theory. *Remote Sensing of Environment*, 112(12), pp.4333-4343.
- Garrigues, S., Shabanov, N.V., Swanson, K., Morisette, J.T., Baret, F. and Myneni, R.B., 2008. Intercomparison and sensitivity analysis of Leaf Area Index retrievals from LAI-2000, AccuPAR, and digital hemispherical photography over croplands. *Agricultural and Forest Meteorology*, 148(8), pp.1193-1209.

- Gray, J., Sulla-Menashe, D. and Friedl, M. 2016. 'MODIS Collection 6 Land Cover & Land Cover Dynamics'. 2016 MODIS/VIIRS Science Team Meeting, 6-10 June 2016, Silver Spring, Maryland, USA.
- Global Climate Observing System (GCOS), *Systematic observation requirements for satellitebased products for climate, GCOS-107*, World Meteorol. Organ., Geneva, Switzerland, 2006.
- Houborg, R., Soegaard, H. and Boegh, E., 2007. Combining vegetation index and model inversion methods for the extraction of key vegetation biophysical parameters using Terra and Aqua MODIS reflectance data. *Remote Sensing of Environment*, 106(1), pp.39-58.
- Hu, J., Tan, B., Shabanov, N., Crean, K.A., Martonchik, J.V., Diner, D.J., Knyazikhin, Y. and Myneni, R.B., 2003. Performance of the MISR LAI and FPAR algorithm: A case study in Africa. *Remote Sensing of Environment*, 88(3), pp.324-340.
- Huang, D., Knyazikhin, Y., Dickinson, R.E., Rautiainen, M., Stenberg, P., Disney, M., Lewis, P., Cescatti, A., Tian, Y., Verhoef, W. and Martonchik, J.V., 2007. Canopy spectral invariants for remote sensing and model applications. *Remote Sensing of Environment*, 106(1), pp.106-122.
- Jacquemoud, S., Baret, F. and Hanocq, J.F., 1992. Modeling spectral and bidirectional soil reflectance. *Remote sensing of Environment*, 41(2-3), pp.123-132.
- Justice, C.O., Román, M.O., Csizar, I., Vermote, E.F., Wolfe, R.E., Hook, S.J., Friedl, M., Wang, Z., Schaaf, C.B., Miura, T. and Tschudi, M., 2013. Land and cryosphere products from Suomi NPP VIIRS: Overview and status. *Journal of Geophysical Research: Atmospheres*, 118(17), pp.9753-9765.
- Knorr, W. and Kattge, J., 2005. Inversion of terrestrial ecosystem model parameter values against eddy covariance measurements by Monte Carlo sampling. *Global Change Biology*, 11(8), pp.1333-1351.
- Knyazikhin, Y., Glassy, J., Privette, J.L., Tian, Y., Lotsch, A., Zhang, Y., Wang, Y., Morisette, J.T., Votava, P., Myneni, R.B. and Nemani, R.R., 1999. MODIS leaf area index (LAI) and fraction of photosynthetically active radiation absorbed by vegetation (FPAR) product (MOD15) algorithm theoretical basis document. *Theoretical Basis Document, NASA Goddard Space Flight Center, Greenbelt, MD, 20771*.
- Knyazikhin, Y., Marshak, A. and Myneni, R.B., 2005. 3D radiative transfer in vegetation canopies and cloud-vegetation interaction. In *3D Radiative Transfer in Cloudy Atmospheres* (pp. 617-651). Springer Berlin Heidelberg.
- Knyazikhin, Y., Martonchik, J.V., Diner, D.J., Myneni, R.B., Verstraete, M., Pinty, B. and Gobron, N., 1998b. Estimation of vegetation canopy leaf area index and fraction of absorbed photosynthetically active radiation from atmosphere-corrected MISR data. *Journal of Geophysical Research: Atmospheres*, 103(D24), pp.32239-32256.
- Knyazikhin, Y., Martonchik, J.V., Myneni, R.B., Diner, D.J. and Running, S.W., 1998a. Synergistic algorithm for estimating vegetation canopy leaf area index and fraction of absorbed photosynthetically active radiation from MODIS and MISR data. *Journal of Geophysical Research*, 103(D24), p.32257.
- Knyazikhin, Y., Schull, M.A., Stenberg, P., Möttus, M., Rautiainen, M., Yang, Y., Marshak, A.,

- Carmona, P.L., Kaufmann, R.K., Lewis, P. and Disney, M.I., 2013. Hyperspectral remote sensing of foliar nitrogen content. *Proceedings of the National Academy of Sciences*, 110(3), pp.E185-E192.
- Kuusk, A., Lang, M. and Nilson, T., 2004. Simulation of the reflectance of ground vegetation in sub-boreal forests. *Agricultural and Forest Meteorology*, 126(1), pp.33-46.
- Li, X., Strahler, A.H. and Woodcock, C.E., 1995. A hybrid geometric optical-radiative transfer approach for modeling albedo and directional reflectance of discontinuous canopies. *IEEE Transactions on Geoscience and Remote Sensing*, 33(2), pp.466-480.
- Majasalmi, T., Rautiainen, M., Stenberg, P. and Manninen, T., 2015. Validation of MODIS and GEOV1 fPAR products in a boreal forest site in Finland. *Remote Sensing*, 7(2), pp.1359-1379.
- Morisette, J.T., Baret, F., Privette, J.L., Myneni, R.B., Nickeson, J.E., Garrigues, S., Shabanov, N.V., Weiss, M., Fernandes, R.A., Leblanc, S.G. and Kalacska, M., 2006. Validation of global moderate-resolution LAI products: A framework proposed within the CEOS land product validation subgroup. *IEEE Transactions on Geoscience and Remote Sensing*, 44(7), p.1804.
- Möttus, M. and Stenberg, P., 2008. A simple parameterization of canopy reflectance using photon recollision probability. *Remote Sensing of Environment*, 112(4), pp.1545-1551.
- Myneni, R.B. and Ross, J.K., 1991. Photon-vegetation interaction.
- Myneni, R.B. and Williams, D.L., 1994. On the relationship between FAPAR and NDVI. *Remote Sensing of Environment*, 49(3), pp.200-211.
- Myneni, R.B., Hoffman, S., Knyazikhin, Y., Privette, J.L., Glassy, J., Tian, Y., Wang, Y., Song, X., Zhang, Y., Smith, G.R. and Lotsch, A., 2002. Global products of vegetation leaf area and fraction absorbed PAR from year one of MODIS data. *Remote Sensing of Environment*, 83(1), pp.214-231.
- Myneni, R.B., Keeling, C.D., Tucker, C.J., Asrar, G. and Nemani, R.R., 1997. Increased plant growth in the northern high latitudes from 1981 to 1991. *Nature*, 386(6626), p.698.
- Myneni, R.B., Ramakrishna, R., Nemani, R. and Running, S.W., 1997. Estimation of global leaf area index and absorbed PAR using radiative transfer models. *IEEE Transactions on Geoscience and remote sensing*, 35(6), pp.1380-1393.
- Panferov, O., Knyazikhin, Y., Myneni, R.B., Szarzynski, J., Engwald, S., Schnitzler, K.G. and Gravenhorst, G., 2001. The role of canopy structure in the spectral variation of transmission and absorption of solar radiation in vegetation canopies. *IEEE Transactions on Geoscience and Remote Sensing*, 39(2), pp.241-253.
- Peltoniemi, J.I., Kaasalainen, S., Näränen, J., Rautiainen, M., Stenberg, P., Smolander, H., Smolander, S. and Voipio, P., 2005. BRDF measurement of understory vegetation in pine forests: dwarf shrubs, lichen, and moss. *Remote Sensing of Environment*, 94(3), pp.343-354.
- Richardson, A.D., Anderson, R.S., Arain, M.A., Barr, A.G., Bohrer, G., Chen, G., Chen, J.M., Ciais, P., Davis, K.J., Desai, A.R. and Dietze, M.C., 2012. Terrestrial biosphere models need better representation of vegetation phenology: results from the North American Carbon Program Site Synthesis. *Global Change Biology*, 18(2), pp.566-584.

- Roger, J.C., Vermote, E.F., Devadiga, S. and Ray, J.P. 2016. Suomi-NPP VIIRS Surface Reflectance User's Guide – Version 1. viewed 1 March 2017, from https://viirsland.gsfc.nasa.gov/PDF/VIIRS_Surf_Refl_UserGuide_v1.1.pdf
- Ross, J.K. and Marshak, A.L., 1988. Calculation of canopy bidirectional reflectance using the Monte Carlo method. *Remote Sensing of Environment*, 24(2), pp.213-225.
- Ross, J., 2012. *The radiation regime and architecture of plant stands* (Vol. 3). Springer Science & Business Media.
- Sellers, P.J., Dickinson, R.E., Randall, D.A., Betts, A.K., Hall, F.G., Berry, J.A., Collatz, G.J., Denning, A.S., Mooney, H.A., Nobre, C.A. and Sato, N., 1997. Modeling the exchanges of energy, water, and carbon between continents and the atmosphere. *Science*, 275(5299), pp.502-509.
- Sellers, P.J., Mintz, Y.C.S.Y., Sud, Y.E.A. and Dalcher, A., 1986. A simple biosphere model (SiB) for use within general circulation models. *Journal of the Atmospheric Sciences*, 43(6), pp.505-531.
- Stenberg, P., 1996. Correcting LAI-2000 estimates for the clumping of needles in shoots of conifers. *Agricultural and Forest Meteorology*, 79(1), pp.1-8.
- Stenberg, P., Möttöus, M. and Rautiainen, M., 2016. Photon recollision probability in modelling the radiation regime of canopies—A review. *Remote Sensing of Environment*, 183, pp.98-108.
- Tan, B., Hu, J., Huang, D., Yang, W., Zhang, P., Shabanov, N.V., Knyazikhin, Y., Nemani, R.R. and Myneni, R.B., 2005. Assessment of the broadleaf crops leaf area index product from the Terra MODIS instrument. *Agricultural and Forest Meteorology*, 135(1), pp.124-134.
- Taylor, K.E., Stouffer, R.J. and Meehl, G.A., 2012. An overview of CMIP5 and the experiment design. *Bulletin of the American Meteorological Society*, 93(4), pp.485-498.
- Tian, Y., Woodcock, C.E., Wang, Y., Privette, J.L., Shabanov, N.V., Zhou, L., Zhang, Y., Buermann, W., Dong, J., Veikkanen, B. and Häme, T., 2002. Multiscale analysis and validation of the MODIS LAI product: I. Uncertainty assessment. *Remote Sensing of Environment*, 83(3), pp.414-430.
- Wang, Y., Tian, Y., Zhang, Y., El-Saleous, N., Knyazikhin, Y., Vermote, E. and Myneni, R.B., 2001. Investigation of product accuracy as a function of input and model uncertainties: Case study with SeaWiFS and MODIS LAI/FPAR algorithm. *Remote Sensing of Environment*, 78(3), pp.299-313.
- Wang, Y., Buermann, W., Stenberg, P., Smolander, H., Häme, T., Tian, Y., Hu, J., Knyazikhin, Y. and Myneni, R.B., 2003. A new parameterization of canopy spectral response to incident solar radiation: Case study with hyperspectral data from pine dominant forest. *Remote Sensing of Environment*, 85(3), pp.304-315.
- Weiss, M., Baret, F., Block, T., Koetz, B., Burini, A., Scholze, B., Lecharpentier, P., Brockmann, C., Fernandes, R., Plummer, S. and Myneni, R., 2014. On Line Validation Exercise (OLIVE): A web based service for the validation of medium resolution land products. Application to FAPAR products. *Remote Sensing*, 6(5), pp.4190-4216.
- Xiong, X., Butler, J., Chiang, K., Efremova, B., Fulbright, J., Lei, N., McIntire, J., Oudrari, H., Sun, J., Wang, Z. and Wu, A., 2014. VIIRS on-orbit calibration methodology and

- performance. *Journal of Geophysical Research: Atmospheres*, 119(9), pp.5065-5078.
- Yan, K., Park, T., Yan, G., Chen, C., Yang, B., Liu, Z., Nemani, R.R., Knyazikhin, Y. and Myneni, R.B., 2016a. Evaluation of MODIS LAI/FPAR product collection 6. Part 1: Consistency and improvements. *Remote Sensing*, 8(5), p.359.
- Yan, K., Park, T., Yan, G., Liu, Z., Yang, B., Chen, C., Nemani, R.R., Knyazikhin, Y. and Myneni, R.B., 2016b. Evaluation of MODIS LAI/FPAR Product Collection 6. Part 2: Validation and Intercomparison. *Remote Sensing*, 8(6), p.460.
- Yang, W., Shabanov, N.V., Huang, D., Wang, W., Dickinson, R.E., Nemani, R.R., Knyazikhin, Y. and Myneni, R.B., 2006. Analysis of leaf area index products from combination of MODIS Terra and Aqua data. *Remote Sensing of Environment*, 104(3), pp.297-312.
- Zhu, Z., Bi, J., Pan, Y., Ganguly, S., Anav, A., Xu, L., Samanta, A., Piao, S., Nemani, R.R. and Myneni, R.B., 2013. Global data sets of vegetation leaf area index (LAI) 3g and Fraction of Photosynthetically Active Radiation (FPAR) 3g derived from Global Inventory Modeling and Mapping Studies (GIMMS) Normalized Difference Vegetation Index (NDVI3g) for the period 1981 to 2011. *Remote Sensing*, 5(2), pp.927-948.